Tracking Deep Sediment Underplating in a Fossil Subduction Margin: Implications for Interface Rheology and Mass and Volatile Recycling

Author(s):
Tewksbury-Christle, Carolyn M.; Behr, Whitney M.; Helper, Mark A.

Publication date:
2021-03

Permanent link:
https://doi.org/10.3929/ethz-b-000477597

Originally published in:
Geochemistry, Geophysics, Geosystems 22(3), https://doi.org/10.1029/2020GC009463

Geochemistry, Geophysics, Geosystems

RESEARCH ARTICLE
10.1029/2020GC009463

Tracking Deep Sediment Underplating in a Fossil Subduction Margin: Implications for Interface Rheology and Mass and Volatile Recycling

C. M. Tewksbury-Christle[1,2], W. M. Behr[1,2], and M. A. Helper[2]

[1]Structural Geology and Tectonics Group, Department of Geosciences, Geological Institute, ETH Zurich, Zurich, Switzerland, [2]Department of Geological Sciences, Jackson School of Geosciences, University of Texas at Austin, Austin, TX, USA

Key Points:

- The Condrey Mountain Schist fossil subduction interface records distributed deformation across a 2+ km dominantly sedimentary shear zone
- Subduction erosion of the overriding plate sourced ultramafic lenses, which were subsequently entrained and underplated at depth
- Periodic strain localization to the margins of km-scale ultramafic lenses facilitated decoupling from the downgoing slab and underplating

Supporting Information:

- Supporting Information S1

Correspondence to:

C. M. Tewksbury-Christle, carolyn.tewksbury-christle@erdw.ethz.ch

Citation:

Tewksbury-Christle, C. M., Behr, W. M., & Helper, M. A. (2021). Tracking deep sediment underplating in a fossil subduction margin: Implications for interface rheology and mass and volatile recycling. *Geochemistry, Geophysics, Geosystems*, *22*, e2020GC009463. https://doi.org/10.1029/2020GC009463

Received 5 OCT 2020
Accepted 7 FEB 2021

Abstract The architecture and mechanical properties of the subduction interface impact large-scale subduction processes, including mass and volatile recycling, upper-plate orogenesis, and seismic behavior. The nature of the deep subduction interface, where a dominantly frictional megathrust likely transitions to a distributed ductile shear zone, is poorly understood, due to a lack of constraints on rock types, strain distribution, and interface thickness in this depth range. We characterized these factors in the Condrey Mountain Schist, a Late Jurassic to Early Cretaceous subduction complex in northern California that consists of an upper and lower unit. The Lower Condrey unit is predominantly pelagic and hemipelagic metasediment with m-to km-scale metamafic and metaserpentinitic ultramafic lenses all deformed at epidote blueschist facies (0.7–1.1 GPa, 450°C). Major and trace element geochemistry suggest tectonic erosion of the overriding plate sourced all ultramafic and some mafic lenses. We identified two major ductile thrust zones responsible for Lower Condrey unit assembly, with earlier strain distributed across the structural thickness between the ductile thrusts. The Lower Condrey unit records distributed deformation across a sediment-dominated, 2+ km thick shear zone, possibly consistent with low velocity zones observed in modern subduction zones, despite subducting along a sediment poor, tectonically erosive margin. Periodic strain localization occurred when rheological heterogeneities (i.e., km-scale ultramafic lenses) entered the interface, facilitating underplating that preserved 10%–60% of the incoming sediment. Modern mass and volatile budgets do not account for erosive margin underplating, so improved quantification is crucial for predicting mass and volatile net flux to Earth′s interior.

Plain Language Summary Subduction zones host the largest earthquakes in the world, along with other complex seismic behavior, and are major pathways for recycling to Earth's interior. The subduction interface governs these processes, but its role depends on both rock type and how deformation is distributed. The interface characteristics deeper than where subduction zone earthquakes occur remain unclear. Modern subduction zone evidence suggests that the interface might be narrow or several kilometers thick and might be occupied by sedimentary or igneous rocks, or a combination. To help resolve these uncertainties, we investigated fossil subduction interfaces in the Condrey Mountain Schist, northern California. The Condrey Mountain Schist consists of subducted rocks added to the overriding plate and later brought back to the surface. These fossil interfaces vary with time from several kilometers thick in dominantly originally sedimentary rocks to meters to tens of meters thick in wholly ultramafic rocks. These ultramafic rocks were sourced from the overriding plate. Knowing subduction interface characteristics allows researchers to better understand complex modern seismic behavior. The Condrey Mountain Schist also preserves 10%–60% of the incoming sediment. Current predictions of recycling to Earth's interior do not account for this type of preservation and may overestimate recycled amounts.

1. Introduction

The deep subduction interface is a shear zone composed of relatively weak material that accommodates convergent motion between overriding and downgoing plates in a subduction zone (Cloos & Schreve, 1988). This shear zone plays a key role in subduction dynamics and global processes, including, for example: interplate coupling and upper plate deformation (e.g., Agard et al., 2018; Behr & Becker, 2018; Fagereng & Ellis, 2009; Sage et al., 2006); transient seismic and aseismic slip behaviors (e.g., Audet & Kim, 2016; Audet

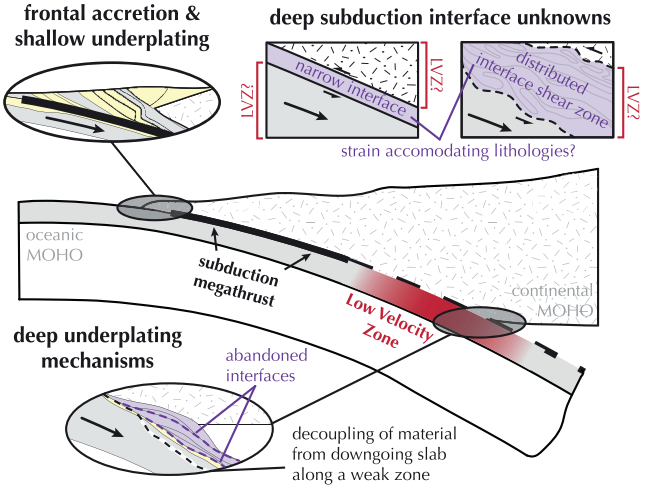

Figure 1. Schematic sketch of transitions in subduction interface architecture with depth. The subduction interface transitions downdip from a fault or set of fault strands capable of hosting megathrust earthquakes to a deeper interface characterized by anomalous seismic velocities (low velocity zone, LVZ, red) and transient seismic and aseismic slip events (e.g., low frequency earthquakes, slow slip events, and episodic tremor and slow slip). The rock record can help to reconcile uncertainties about the lithologies occupying the deep interface, strain distribution, and spatial relationship to the LVZ (upper boxes). Deep underplating (bottom oval) helps to preserve a record of subduction interface processes, but the mechanisms (namely what constitutes the weak zone that facilitates decoupling from the slab and underplating, black dashed line) remain unclear.

& Schaeffer, 2018; Fagereng & Sibson, 2010; Saffer & Wallace, 2015); and mass and volatile recycling to the deep interior (e.g., Clift et al., 2009; Jarrard, 2003; Kerrick & Connolly, 2001).

The mechanical properties of subduction interface shear zones inevitably evolve as a function of subducted materials and the pressure-temperature (P-T) conditions they reach during progressive subduction. One of the primary manifestations of rheological changes with depth in modern subduction zones is the rich spectrum of seismic and aseismic transient deformation patterns recorded along the interface at different locations. At shallow depths, for example, many subduction zones exhibit slow slip events that are sometimes accompanied by tectonic tremor (e.g., Nakano et al., 2018; Saffer & Wallace, 2015; Todd et al., 2018). The shallow interface transitions down-dip to a locked zone—a discrete fault or multi-strand fault zone capable of hosting megathrust earthquakes (e.g., Agurto et al., 2012; Lay et al., 2005, 2012; Rowe et al., 2013). Increasing P-T conditions even farther downdip may promote a switch to dominantly viscous deformation (Figure 1) (e.g., Behr & Platt, 2013; Kotowski & Behr, 2019; Stöckhert et al., 1999; Tarling et al., 2019), and these deeper sections of the interface host similar behavior to the shallow regions in the form of slow slip events, low frequency earthquakes, and episodic tremor and slow slip (Audet & Kim, 2016; Beroza & Ide, 2009; Obara & Hirose, 2006; Rogers & Dragert, 2003).

The transition between the dominantly frictional megathrust and the deeper interface shear zone in subduction environments is especially poorly understood. Two primary open questions that remain are as follows: 1) what are the rock types that occupy the subduction interface at these depths and 2) how is strain distributed and/or localized amongst them?

The seismological record from modern subduction zones provides some clues but also highlights several ambiguities. Many subduction margins, for example, have a 3–5-km-thick low seismic velocity zone (LVZ) downdip of the subduction megathrust (Audet & Kim, 2016; Bostock, 2013, and references therein, Figure 1). Collocation of the LVZ with transient slip events suggests that it may be related to the subduction interface, but the data are consistent with both a narrow discrete shear zone above or below the LVZ (Calvert et al., 2020; Hansen et al., 2012; Kurashimo et al., 2013) or a broadly distributed shear zone that encompasses the LVZ (Figure 1) (Audet & Schaeffer, 2018; Bostock, 2013; Calvert et al., 2020; Delph et al., 2018; Nedimović et al., 2003). Lithologies responsible for the LVZ are similarly unclear, with velocities consistent with overpressurized dominantly mafic rocks (Audet & Schaeffer, 2018; Bostock, 2013; Hansen et al., 2012), dominantly sedimentary rocks (Abers et al., 2009; Calvert et al., 2011), or a combination of both (Bostock, 2013; Delph et al., 2018).

Exhumed subduction complexes also provide some clues as to the nature of the deep subduction interface. These complexes capture subduction interface processes through tectonic underplating, which is the process of separation of material from the downgoing slab along zones of weakness and the associated transfer of detached slices to the upper plate (Figure 1). Multiple subduction complexes exhumed from both shallow and great depths show evidence for this process, exhibiting coherent, repeated, oceanic and sedimentary slices with downward-younging metamorphic ages (Agard et al., 2018; Angiboust et al., 2018; Dumitru et al., 2010; Kitamura & Kimura, 2012; Monie & Agard, 2009; Platt, 2015; Plunder et al., 2013). Along the shallow interface, decoupling from the slab typically occurs via localization along a weak décollement within or at the base of the sediment pile that facilitates imbrication and basal accretion of additional incoming sediments (Figure 1) (e.g., Davis et al., 1983; Graveleau et al., 2012; Kimura & Ludden, 1995). The distribution of weak layers within the sediment pile, as well as the rheology of the décollement, govern internal deformation within the packages (e.g., Davis et al., 1983; Graveleau et al., 2012; Konstantinovskaya & Malavieille, 2011; Ruh, 2020; Ruh et al., 2012; Yamato et al., 2011). Deep decoupling (separation of material) of

coherent tectonic slices similarly requires strain localization onto weak zones within the downgoing slab, where subsequent mechanical coupling to the overriding plate drives underplating (Agard et al., 2018), but mechanisms for generating the weak décollement, its relative location (e.g., in the sediment pile vs. in the downgoing slab mantle or crust), and controls on the thicknesses of underplated packages are much less well constrained. A better understanding of deep underplating processes is essential to making predictions about the rock types typically stranded on the deep interface, and their propensity to affect permeability and fluid flow, to control seismic velocities, and to host transient slip events (cf., Behr & Burgmann, 2020).

Placing better constraints on the underplating processes that strand materials on the deep subduction interface is not only essential to understanding subduction interface properties and rheology, but may also impact mass and volatile budgets relevant to quantifying continental growth and carbon cycling. Subduction zones serve as major pathways for recycling mass and volatiles to the Earth's interior (e.g., Clift et al., 2009; Jarrard, 2003; Kerrick & Connolly, 2001). Long-term cratonic and atmospheric stability suggest that continental mass and carbon budgets should be relatively balanced, with negative and positive fluxes approximately equal, consistent with current budgets (Clift et al., 2009; Mason et al., 2017). Current carbon budgets, however, omit deep underplating as a possible reservoir for preserving mass and volatiles (Clift, 2017; Clift et al., 2009) despite geophysical (Bassett et al., 2010; Calvert et al., 2020; T. Ito et al., 2009), geomorphic (Clift & Hartley, 2007; Litchfield et al., 2007), modeling (e.g., Menant et al., 2020), and rock record (e.g., Agard et al., 2018; Aoki et al., 2009; Dumitru et al., 2010; Kotowski & Behr, 2019) evidence. Previously published underplating estimates from modern subduction zones can be as high as 80% of the incoming sediment, representing a significant reduction of total negative flux (Clift & Hartley, 2007). Quantitatively estimating the relative contributions of deep underplating as a mass and/or volatile reservoir requires an understanding of the structural architecture at subduction margins, namely what structures facilitate underplating and what is the relative material storage due to underplating.

In this paper, we utilize a well exposed, prograde blueschist facies subduction complex to unravel deep subduction and underplating processes, and to explore implications for both the rheology of subduction interface shear zones and the degree to which they sequester mass and volatiles and influence continental recycling. The Condrey Mountain Schist is a Late Jurassic to Early Cretaceous exhumed subduction complex in northern California and southern Oregon (Figures 2 and 3) (Helper, 1986; Saleeby & Harper, 1993; Snoke & Barnes, 2006). The schist exposes nearly 15 km of structurally stacked, oceanic-affinity, sedimentary, mafic, and ultramafic protoliths metamorphosed to epidote-amphibolite, greenschist, and epidote-blueschist facies (Coleman & Helper, 1983; Donato et al., 1980; Helper, 1986). Our approach is to combine detailed structural mapping and geochemistry to identify a) the provenance of different protoliths in the schist unit, b) the structures and fabrics responsible for underplating within individual schist slices, and c) the lateral and temporal evolution of rheology amongst heterogeneous lithologies.

2. Geologic Setting

The western North American margin records 300+ m.y. of subduction in the Klamath Mountains (Figure 2a) and the Franciscan accretionary complex (Figure 2b) (Dickinson, 2004). The most well-known and well-studied signature of that subduction is the Middle Jurassic to Oligocene Franciscan accretionary complex, the Great Valley Group, and the Sierra Nevada batholith, which together represent a fossil wedge-forearc basin-arc system (Figure 2b) (Hamilton, 1969). Subduction initiation ca. 164-170 Ma is inferred from the ages of the Coast Range Ophiolite (Hopson et al., 2008) and the oldest high pressure-low temperature blocks in the Franciscan Central Belt mélange (Wakabayashi, 1990), but the early history is nonaccretionary with initial underplating in the Franciscan complex beginning ca. 123 Ma, coincident with an increase in volcanism in the Sierra Nevada arc that marked establishment of through-going oceanic-continental subduction along the western North American margin (Dumitru et al., 2010). The Klamath Mountains (Figure 2a, Section 2.1) in northern California and southern Oregon, are inboard of the Franciscan complex and predominantly pre-date subduction initiation (e.g., Snoke & Barnes, 2006). However, the latest stages of Klamath development overlap with the early Franciscan history, with the Josephine Ophiolite forming ca. 160-170 Ma (Harper et al., 1994), comparable to the Coast Range Ophiolite, and Mesozoic intrusions common throughout the Klamath terranes. Underplating of the Condrey Mountain Schist (Figure 3, Section 2.2) beneath the Klamath terranes began at 155 ± 5 Ma (Hacker et al., 1995; Saleeby & Harper, 1993),

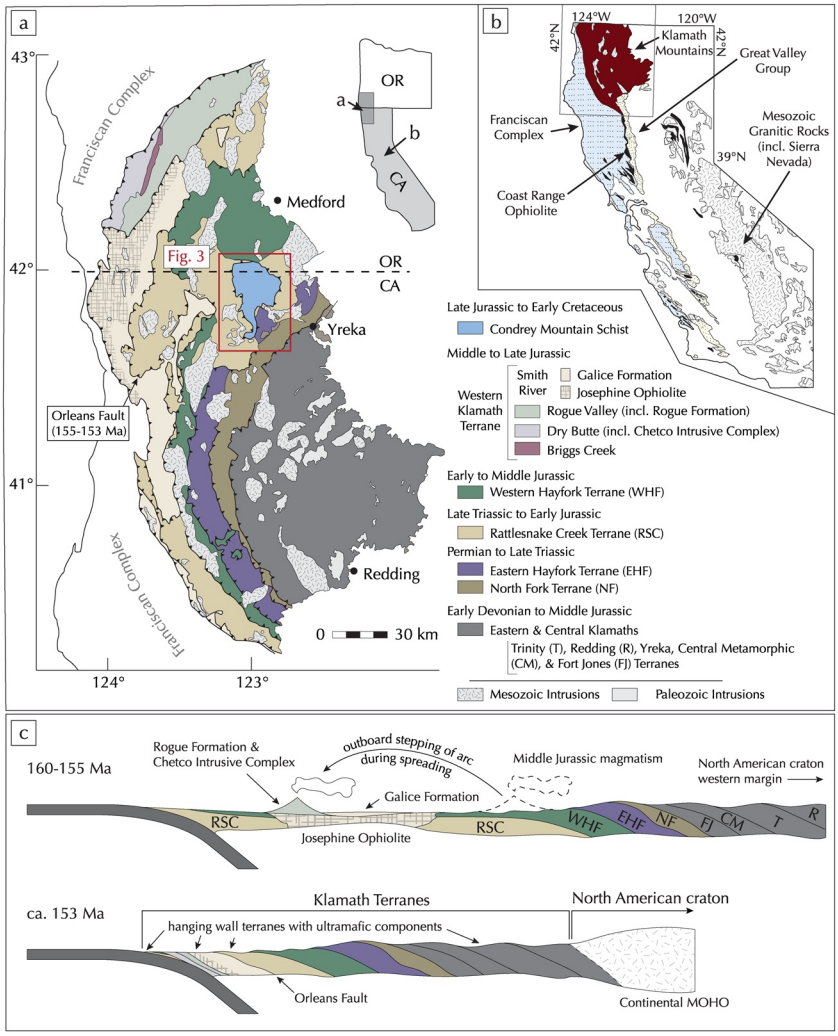

Figure 2. Geologic map and tectonic reconstructions of the Klamath Mountains in northern California and southern Oregon. (a) Map modified from Snoke and Barnes (2006). (b) Generalized tectonic sketch map of the western North American margin in California showing the relationships between the Klamath Mountains (red) and the Franciscan accretionary complex (blue with linear dots), Great Valley Group (yellow with scattered dots), Coast Range ophiolite (black), and Mesozoic granitic rocks (including the Sierra Nevada, gray with crosshatches) (after Ernst, 2015). (c) Tectonic reconstructions showing Klamath tectonics after spreading to form the Josephine Ophiolite (top) and immediately after thrusting along the Orleans fault (bottom). Dashed lines for Middle Jurassic magmatism mark arc location prior to outboard stepping of the active arc.

approximately coeval to final assembly of the Klamath terranes (ca. 153-150 Ma, Snoke and Barnes, 2006). This underplating, initially documented by Helper (1986), falls within the early Franciscan non-accretionary history.

2.1. Klamath Mountains

The Klamath Mountains are composed of a series of eastward-dipping, westward-younging thrust sheets that suture the remnants of multiple fringing island arc, forearc, and accretionary wedge systems onto the western margin of North America (Figure 2) (e.g., Gray, 1986; Hacker et al., 1995; Pessagno, 2006; Saleeby, 1990; Saleeby & Harper, 1993; Snoke & Barnes, 2006; Wright & Wyld, 1994; Yule et al., 2006). These terranes are generally inboard of and older than the Franciscan accretionary complex (Dumitru et al., 2010) and record subduction along multiple trenches from the Early Devonian through Late Jurassic (e.g., Hacker et al., 1995; Saleeby, 1990; Saleeby & Harper, 1993; Snoke & Barnes, 2006; Wright & Wyld, 1994). The

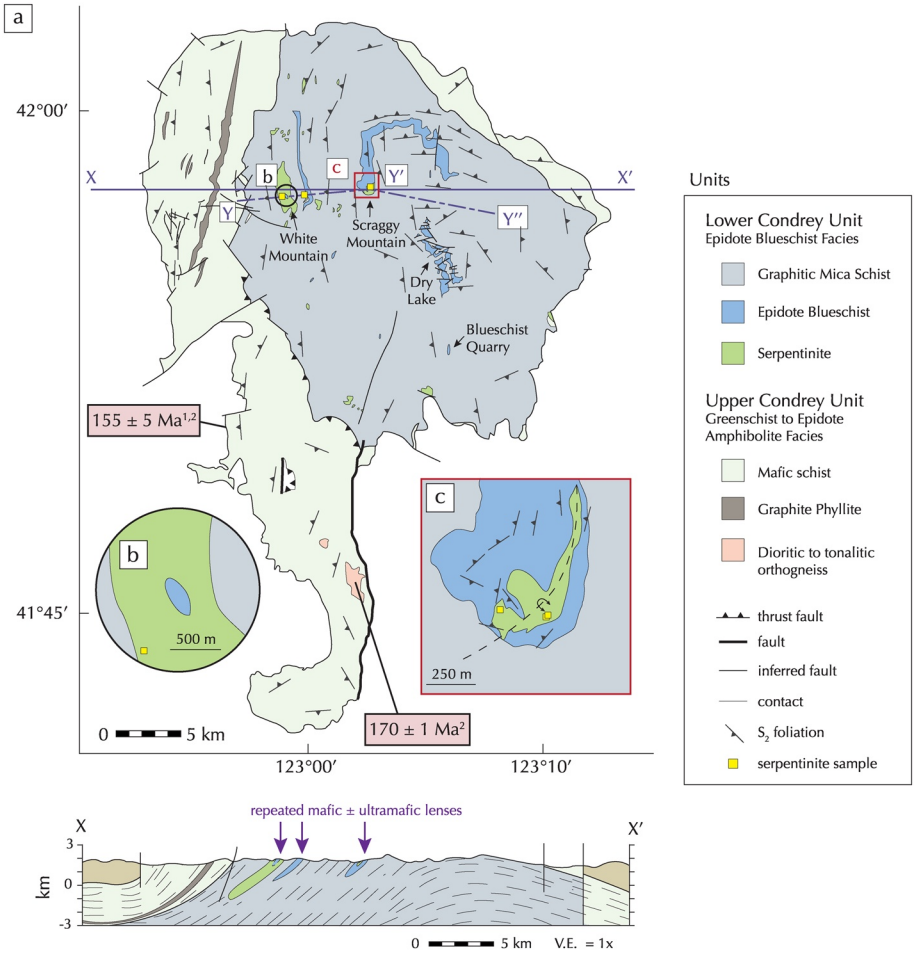

Figure 3. (a) Geologic map and cross-section of the Condrey Mountain Schist, modified from Helper (1985). Age data are from Hacker et al. (1995)[1] and Saleeby and Harper (1993)[2]. The black circle marks the White Mountain serpentinite body (inset b) and the red box marks Scraggy Mountain (inset c), discussed in Section 4. Yellow boxes mark serpentinite geochemistry samples, discussed in Section 3. The purple dashed line (Y-Y'-Y") shows the cross-section line depicted in Figure 10.

Condrey Mountain Schist occupies a window through the Klamath terranes that exposes the youngest and structurally deepest portion of the Klamath province (Figures 2a and 3) (Helper, 1986).

The Condrey Mountain Schist is primarily in thrust contact with an ophiolitic melange (Rattlesnake Creek terrane), but is locally juxtaposed against a west-facing arc with associated plutons (Western Hayfork terrane) and a fossil accretionary wedge (Eastern Hayfork terrane) (Figures 2a and 2c) (C. G. Barnes et al., 2006, 2020; Frost et al., 2006; Gray, 1986; Hacker et al., 1995; Helper, 1986; Snoke & Barnes, 2006; Wright, 1982; Wright & Wyld, 1994). These terranes sutured to the inboard Klamath terranes ≥170 Ma (Saleeby, 1990; Snoke & Barnes, 2006), but plutons that cross-cut the terrane bounding thrusts suggest ongoing arc activity over an east-dipping slab (Figure 2c) (Wright & Wyld, 1994). Subsequent transtensional spreading in the overriding plate nearly parallel to the margin dissected the Rattlesnake Creek, forming the Josephine Ophiolite in the resulting basins (165-161 Ma, Figures 2a and 2c) (Hacker et al., 1995; Saleeby & Harper, 1993; Snoke & Barnes, 2006; Yule et al., 2006). The active arc stepped outboard during spreading (Snoke & Barnes, 2006; Yule et al., 2006), but the arc volcanics (Rogue Valley and Dry Butte subterranes) are only preserved in the NW Klamaths. Thrusting ca. 153-150 Ma closed the Josephine basins and assembled the remaining outboard Klamath terranes (Figure 2c) (Frost et al., 2006; Saleeby, 1990; Snoke & Barnes, 2006).

2.2. Condrey Mountain Schist

The Condrey Mountain Schist occupies a subcircular structural window centered on a long-wavelength Neogene dome that overprints the Klamath terranes (Helper, 1986; Mortimer & Coleman, 1985). Pervasive transposition foliations in the Condrey Mountain Schist define an asymmetric dome with steeply dipping western and more gently dipping northern, eastern, and southern limbs (Figure 3), consistent with the larger-scale Klamath dome. This late-stage doming exposes nearly 15 km of Condrey Mountain Schist structural thickness (Figure 3).

The Condrey Mountain Schist consists of epidote-amphibolite to epidote-blueschist facies metasedimentary, metamafic, and metaserpentinitic ultramafic rocks (Helper, 1986). An epidote-amphibolite to greenschist facies unit (Upper Condrey unit) crops out along the western and northeastern edges of the Condrey Mountain Schist window, locally defining an inverted metamorphic gradient that decreases in grade from the window margins inward (Helper, 1986). The epidote-blueschist facies unit (Lower Condrey unit) in the center of the dome is juxtaposed against the Upper Condrey unit along predominantly high angle faults that cut ductile fabrics in both the Lower and Upper Condrey units. Previous structural characterization by Helper (1986) identified multiple generations of ductile deformation in both units.

The Upper Condrey unit consists of predominantly greenschist facies (0.3–0.5 GPa, 300°C–400°C) metavolcanic rocks, intercalated with m-to km-scale lenses of graphite phyllite (Helper, 1986). U-Pb crystallization ages for concordant dioritic to tonalitic orthogneiss lenses within the Upper Condrey unit (Figure 3) indicate that some of the Upper Condrey unit is older than 170 Ma (Saleeby & Harper, 1993). K-Ar hornblende and U-Pb zircon dates for Rattlesnake Creek terrane diorites that are cut by the window-bounding thrust along the northern and western window margins, combined with cooling ages in the surrounding Rattlesnake Creek terrane (Hacker et al., 1995), constrain thrusting to ca. 155 ± 5 Ma (Saleeby & Harper, 1993), approximately coeval with final Klamath assembly.

The structurally lower Lower Condrey unit composes the majority of the Condrey Mountain Schist structural thickness. Peak P-T conditions from mineral stability are within the epidote-blueschist facies (0.7–1.1 GPa, 400°C–450°C; pressure revised from Helper (1986) based on Evans (1990) and updated cymrite and deerite stability of Graham et al. (1992) and Lattard and Le Breton (1994), respectively). The presence of cymrite and deerite bounds the pressure to 0.65–1.3 GPa (Graham et al., 1992; Lattard & Le Breton, 1994), but deerite constraints are for end-member compositions with solid solution effects currently unconstrained. The presence of albite and quartz and absence of jadeite (Helper, 1986), however, constrain maximum pressure to <1.1 GPa at these temperatures (Evans, 1990). Predominantly metasedimentary rocks (graphitic quartz mica schist) are intercalated with m- to km-scale metamafic (epidote blueschist) and serpentinized ultramafic (metaserpentinite) lenses. Graphitic mica schist protoliths are hemipelagic to pelagic sediment (Helper, 1986). The cumulative structural thickness of the Lower Condrey unit graphitic mica schist (Figure 3 cross-section), in conjunction with inward and downward repetitions of metasedimentary, metamafic, and serpentinized ultramafic rock sequences (Figure 3), is suggestive of an episodic history of successive underplating, but the thicknesses of underplated packages and the structures responsible are not constrained. Narrow or absent mafic components between the sedimentary and ultramafic protoliths raise further questions about ultramafic sources (e.g., slicing from the downgoing slab vs. tectonic erosion of the copious ultramafic terranes in the Klamath hanging wall) and the validity of assigning each ultramafic and/or mafic lens to an individual underplated slice.

The Condrey Mountain Schist exhibits very limited evidence for post-peak retrogression or overprinting structures, which allows for excellent preservation of the prograde deformation history. Previous work in the Dry Lake region (Figure 3) identified: 1) pervasive transposition foliation development (D_1), 2) tight to isoclinal folding (D_{2-3}), and 3) boudinage and flattening (D_4) (Helper, 1986). Similar overprinting fabric relationships and deformation styles between and within other lithologic packages (e.g., graphitic mica schist + epidote blueschist + metaserpentinite at Scraggy Mountain, red box, Figure 3) are, however, not as well documented.

3. Geochemistry

3.1. Methods

The mafic and ultramafic material incorporated into the Condrey Mountain Schist had multiple possible sources from both the overriding and downgoing plates. To develop an integrated tectonic history for the Lower Condrey unit, we used major, minor, and trace element geochemistry to fingerprint protolith sources for the epidote blueschist and serpentinized ultramafics.

For epidote blueschist samples, we interpreted published whole rock Ti-V and Zr-Zr/Y compositions (C. G. Barnes et al., 1995). For the metaserpentinites (Figure 3), we analyzed Cr#, Mg#, TiO_2, and Al_2O_3 (cf., J. D. Barnes et al., 2013; Macdonald et al., 2006) of relict chrome spinels on ETH Zurich's Electron Probe Microanalyser using standard coated, microprobe polished, petrographic thin sections. Standards for instrument calibration are detailed in the raw data spreadsheets (see Data Availability Statement). For each of the five samples, we averaged analyses with 99%–101% totals after a standard charge balance.

3.2. Results

Relict chrome spinels from metaserpentinite lenses have Cr# > 0.56 and a range of Mg# (0.1–0.55) (Figure 4a). Samples with high Cr# and low Al_2O_3% (≤20%) are outside the abyssal peridotite field but inside both the forearc peridotite field and the fields defined by Josephine Ophiolite or Rattlesnake Creek chrome spinel geochemistry (dashed, green, and purple in Figures 4a and 4b). Mg# in these samples is either within the forearc peridotite, Josephine Ophiolite, and Rattlesnake Creek terrane fields or outside all defined fields. One sample plots just within the overlap of the forearc and abyssal periodite fields.

Epidote blueschist analyses from the Scraggy Mountain epidote blueschist lens and Dry Lake (Figures 3 and 4c; data from C. G. Barnes et al., 1995) plot in IAB and MORB fields, respectively, on Ti versus V. Additional data from a blueschist quarry (Figures 3 and 4c) plot in the MORB field, similar to Dry Lake. On Zr versus Zr/Y plots (after Pearce & Norry, 1979; Shervais, 1982) (Figure 4d), the majority of the Scraggy Mountain epidote blueschists plot in the overlap between IAB and MORB fields, whereas the majority of Dry Lake samples plot in the MORB field. Samples from the blueschist quarry plot in the MORB field.

Smaller symbols in Figures 4c and 4d show the variety of geochemical signatures of the Klamath terranes that sit outboard of the Condrey Mountain Schist. The outboard Klamath terranes have a range of IAB and MORB affinity geochemical signatures in the Ti versus V plot that overlap with the Condrey Mountain Schist geochemistries (Figure 4c). On Zr versus Zr/Y plots (Figure 4d), the outboard Klamath terranes have geochemistries consistent with IAB, MORB, and OIB sources, but Zr concentrations are higher in the Dry Lake and Blueschist quarry locations (yellow and orange circles), on average, than the outboard Klamath terranes (smaller symbols).

4. Field Observations and Structural Data

We conducted detailed structural mapping to map deformation styles and phases along a roughly strike-perpendicular transect (Y-Y'-Y", Figure 3) that crosses 10+ km of structural thickness. We focused particularly on fabric development proximal to mafic and ultramafic slices (cross-section, Figure 3a), which are plausible boundaries of underplated packages, to characterize any structures involved with underplating.

We group the field and structural data presented below by deformation event (D_1–D_4) based on field classifications. We defined S_2 in the field as the pervasively developed foliation in epidote blueschists, chlorite schists, and metaserpentinites. Overprinting phases of deformation in these lithologies fold S_2 and locally develop incipient cleavages but do not fully transpose S_2 (Section 4.3). In the graphitic mica schist, S_3 locally transposes S_2, but pervasive crenulations affiliated with D_3 (Section 4.3) overprint the S_2 surface and do not occur on the S_3 surface, allowing us to distinguish between the two where S_2 is not well-preserved. Previous work labeled S_2 as S_T affiliated with a D_1 deformation phase (Helper, 1986). Our current classification combines previously mapped D_{1-2} structures under a D_2 phase. D_3 structures fold or cross-cut the pervasive S_2 fabric and D_2 structures, where preserved.

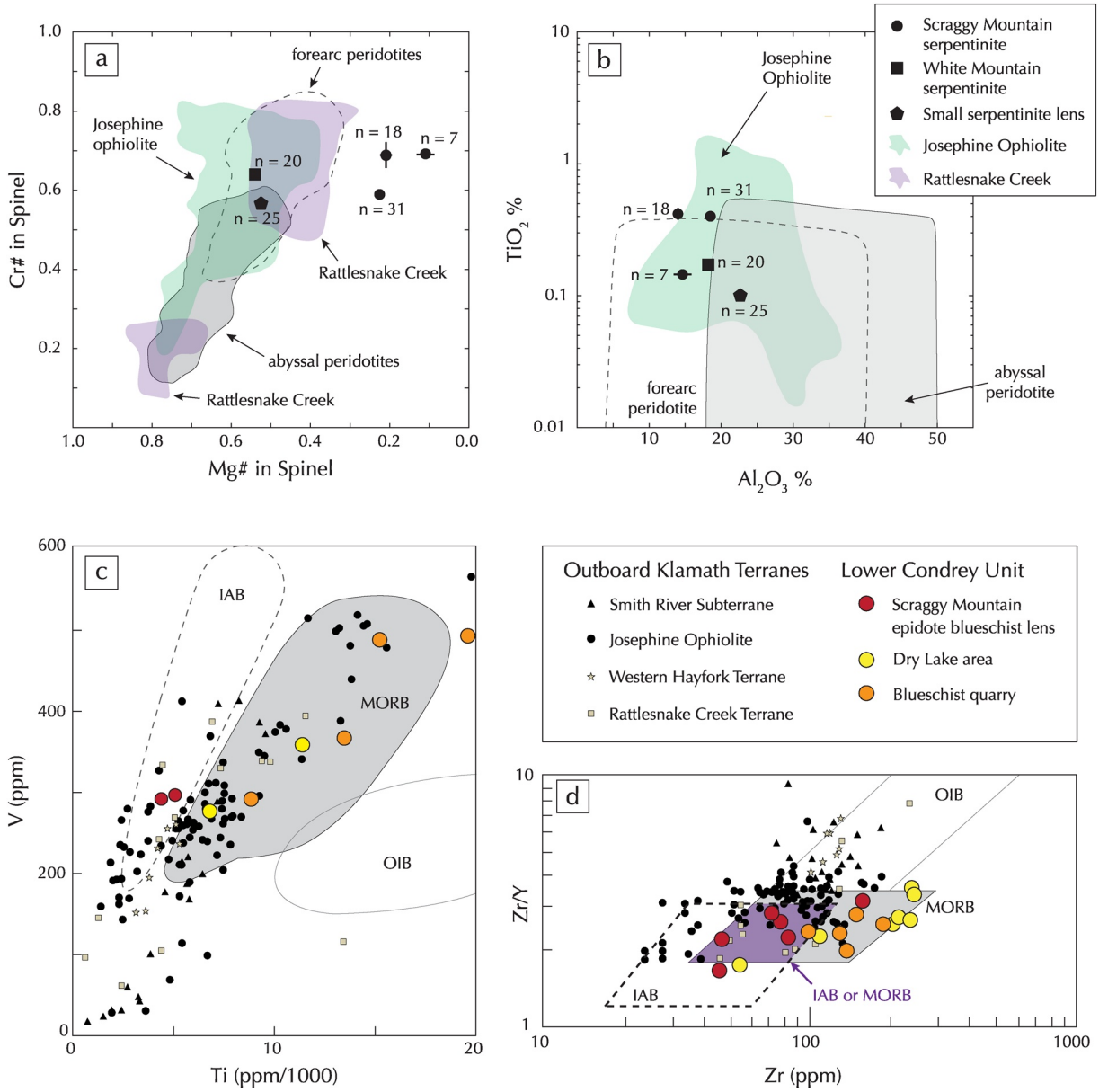

Figure 4. Geochemistry of ultramafic and mafic lenses within the Lower Condrey unit. Raw data for the mafic lenses are from C. G. Barnes et al. (1995). (a) Average Cr# (=Cr/(Cr + Al) atomic ratio) versus Mg# (=Mg/(Mg + Fe^{2+}) atomic ratio) for relict chrome spinels in serpentinized ultramafic lenses from White (squares) Mountain, Scraggy (circles) Mountain, and a small serpentinite lens (pentagon) (Figure 3a) (labeled fields after J. D. Barnes et al., 2013). High Cr# for most analyses is inconsistent with abyssal peridotites (gray field) but is in part consistent with the Josephine Ophiolite (green field) (Macdonald et al., 2006), Rattlesnake Creek terrane (purple field) (Garlick et al., 2009), and other forearc peridotites (dashed field). (b) Average TiO_2% versus Al_2O_3% predominantly fall outside of the abyssal peridotite field (gray) but within the Josephine Ophiolite field (green) and forearc peridotite (dashed) fields (labeled fields after Macdonald et al., 2006). One sample plots just within the overlap of forearc and abyssal peridotite fields in both plots. (c) Ti versus V (after Shervais, 1982) and (d) Zr versus Zr/Y (after Pearce & Norry, 1979), respectively, are shown for three epidote blueschist lenses: 1) Scraggy Mountain epidote blueschist lens (red circles), an along-strike continuation of Scraggy Mountain, 2) Dry Lake area (yellow circles), and 3) Blueschist quarry (orange circles), an occurrence lithologically similar to Dry Lake. Scraggy Mountain samples plot either within the IAB field (dashed) in both plots or in the overlap between IAB and MORB, whereas Dry Lake and Blueschist quarry samples plot within the MORB field (gray) or in the overlap. Smaller symbols mark the range of geochemical compositions for Klamath terranes directly outboard of the Condrey Mountain Schist.

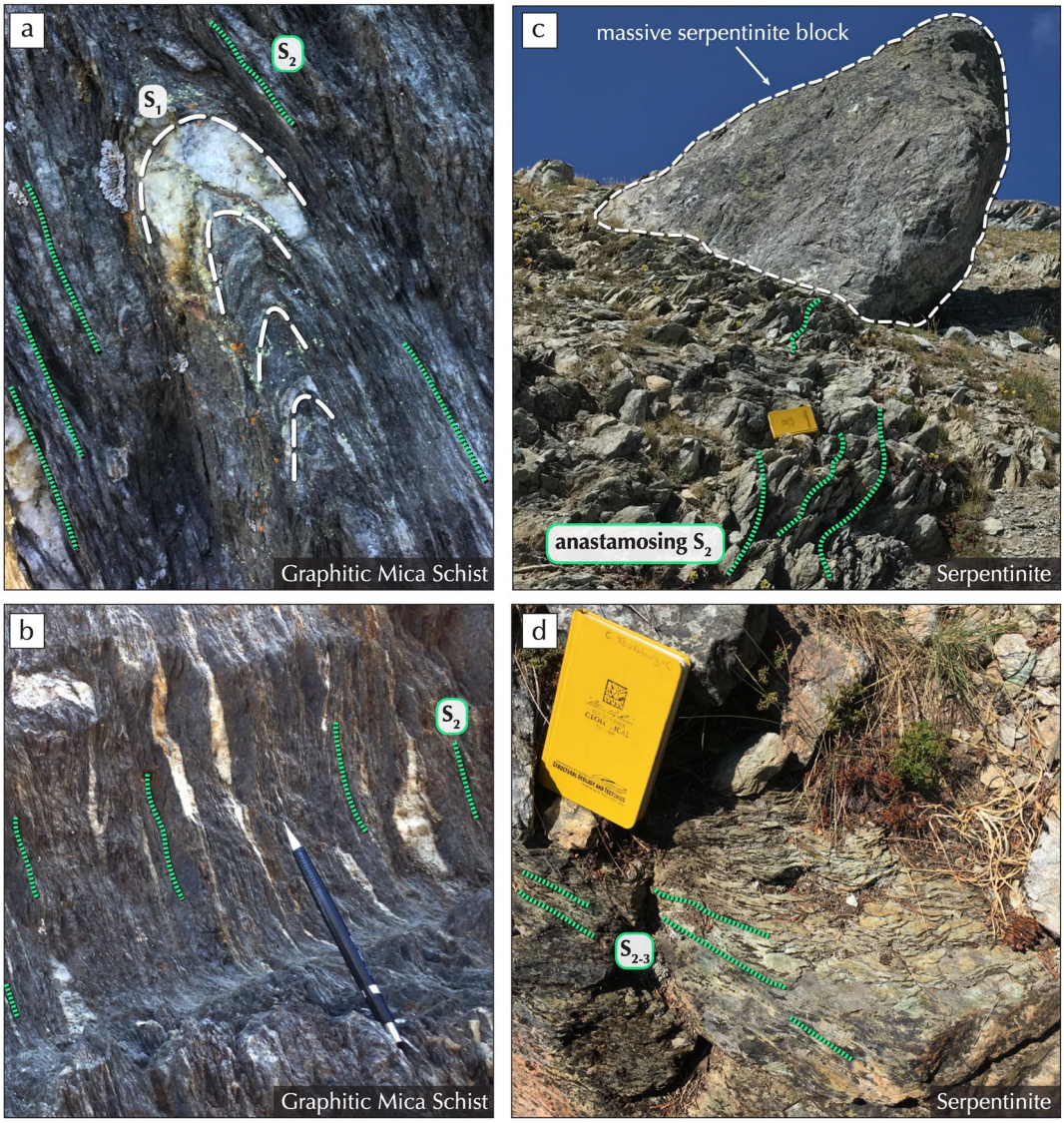

Figure 5. (a) Where preserved, S_1 (dashed white lines) is defined by isoclinally folded, alternating compositional domains crosscut by S_2 (dashed green lines in all images), which is also axial planar to these F_2 folds. (b) S_2 in graphitic mica schist and epidote blueschist is highly planar, pervasive, and defined by alternating compositional domains, here deformed vein quartz. Variation in S_2 orientation defines the map-scale dome. (c) Serpentinite at the core of the White Mountain lens is characterized by anastamosing shear bands (S_2) wrapping around massive m-scale serpentinite blocks (dashed white lines, yellow field notebook for scale). (d) At the base of the White and Scraggy Mountain serpentinite bodies (Figures 3b and 3c, respectively), S_{2-3} folia are coplanar and closely spaced.

We analyzed all structural data (e.g., best fit pi-girdles, fold axis determinations, average orientations) following standard stereographic techniques and using Stereonet 10.2.9 (Allmendinger et al., 2011; Cardozo & Allmendinger, 2013). We reconstructed map-scale structural data (used in Sections 4.3 and 4.4) from measurements of Helper (1985). All new field fabric measurements were obtained with Field Move and/or Field Move Clino.

4.1. D_1

Relict differentiated folia (S_1) are occasionally preserved between foliation planes of the pervasive fabric (S_2, Section 4.2). These hinges between microlithons (crenulation arcs) are at low angles to S_2 (Figure 5a) and,

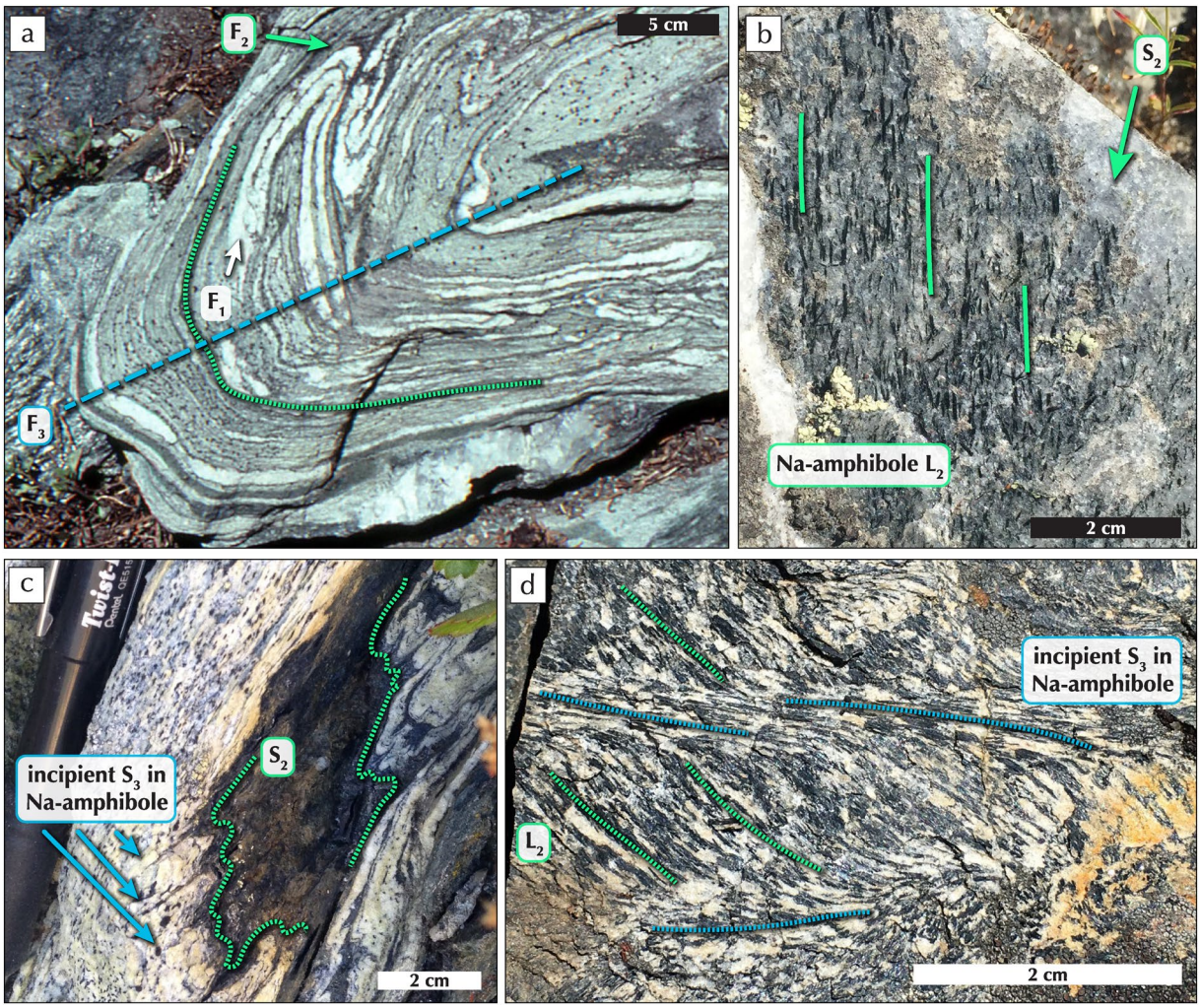

Figure 6. (a) F_3 (blue lines) folding of F_2 (green) and F_1 (white) folds in alternating quartz- and chlorite-epidote-albite layers. (b) S_2 surface with L_2 (green solid line) defined by Na-amphibole. (c) Folded S_2 (green dashed lines) in alternating quartz-albite and Na-amphibole-rich layers with incipient S_3 cleavages defined by Na-amphibole. (d) Na-amphibole L_2 (green) rotating during D_3 folding to form incipient S_3 (blue).

in rare cases, can be traced to refolded isoclinal fold hinges (F_2 overprinting F_1, Figure 6a). Where preserved, D_1 structures are cross-cut and overprinted by D_2 structures (Figure 5a).

4.2. D_2

D_2 forms a pervasively developed transposition foliation (S_2, Figure 3). S_2 is defined by highly elongated Na-amphibole and phengite (defining an L_2 lineation, Figure 6b) or chlorite (in epidote blueschists or chlorite schists, respectively) or by alternating compositional domains (graphitic mica schists and other quartz-rich lithologies). Metamafic and metasedimentary rocks have a well-developed planar, spaced S_2 (Figure 5b). Meter-to decameter-scale epidote blueschist lenses within the graphitic mica schist (Figure 3) have well-developed S_2 with no evidence of strain localization either within or at the margins. The S_2 morphology is more varied in the metaserpentinites. Within the core of the km-scale White Mountain metaserpentinite lens, for example, anastamosing D_2 shear bands wrap m-scale massive metaserpentinite blocks with mineralized brittle fractures (Figure 5c). Within the shear bands themselves, a similar pattern emerges at the cm-to μm-scale, with well-foliated zones wrapping brittley deformed metaserpentinite pods. Some shear bands have a well-developed S-C fabric, but the majority are chaotic with poorly developed stretching lineations. The core of the Scraggy Mountain metaserpentinite lens has similarly massive m-scale blocks but poor exposure prevented further characterization at this location. Over <10 m of structural thickness at

the structural base of the km-scale White and Scraggy Mountain metaserpentinite lenses, folia are coplanar and closely spaced (Figure 5d) and, in the White Mountain lens, are overprinted by a strongly developed rodding lineation and planar crenulation cleavage (S_3, Section 4.3). Because these foliations are consistent with both S_2 or S_3 and foliation development obscures identification of an earlier fabric, we labeled these as S_{2-3}. In contrast, meter-to decameter-scale serpentinite lenses (Figure 3) have no strain localization.

4.3. D_3

S_3 is spatially limited to the Scraggy and White Mountain areas (red square and black circle, respectively, Figure 3). At Scraggy Mountain and across two other transects that cut the Scraggy Mountain epidote blueschist lens, outcrop-scale D_3 structures are observed in the epidote blueschist + metaserpentinite lens as well as within ca. 0.5 km of graphitic mica schist structurally above and below. D_3 folds S_2 surfaces (Figure 6a) and results in incipient S_3 cleavages defined by Na-amphibole rich layers (Figures 6c and 6d).

In the Scraggy Mountain area, a spaced cleavage (S_3) is well-developed in the graphitic mica schist (Figures 7a and 7b). D_3 folds are isoclinal, and S_2 and S_3 are predominantly parallel except proximal to D_3 fold (F_3) hinges (Figure 7c). S_3 crosscuts S_2 where F_3 hinges are preserved (Figure 7c). D_3 folds are tight to open in the epidote blueschist and chlorite schists, however, and S_3 axial planar cleavage is incipient (Figures 7a, 7b, and 7d). F_3 everywhere have s-shaped asymmetry when viewed down-plunge, and S_2 dips more steeply than S_3 on average. Outcrop-scale F_3 orientations (axes and axial planes) and related axial planar cleavage are approximately parallel to the orientations derived from the map-scale moderately plunging, reclined, overturned synform at Scraggy Mountain (Figures 3c and 7e). Crenulation lineations and rare stretching lineations are similarly consistent with the map-scale fold.

In the White Mountain area, an epidote blueschist lens at the core of the White Mountain metaserpentinite has well-developed S_2 overprinted by moderate to tight folds (F_3) and incipient axial planar cleavage (S_3) morphologically similar to structures observed at Scraggy Mountain. Na-amphibole stretching lineations on the limbs of F_3 folds are rotated parallel to F_3 axes proximal to outcrop-scale fold hinges (cf., Figure 6d). Poles to S_2 in the White Mountain lens define several pi-girdles (Figures 8a–8c) that define fold axes that are approximately parallel to directly measured F_3 axes and stretching lineations in epidote blueschist and chlorite schist (Figure 8b). Serpentine stretching lineations are grossly subparallel, but have a larger spread (Figure 8c). Crenulation lineations in the graphitic mica schist below the White Mountain metaserpentinite lens are at a low angle to other F_3 orientations but are collinear to the graphitic mica schist F_3 axis calculated from the graphitic mica schist S_2 pi-girdle (Figure 8a).

4.4. D_4

Doming reorients D_1–D_3 fabrics and structures (see Section 2.2) with local development of kink bands and box folds (F_4) that overprint S_2 and S_3, where developed. Doming is not associated with a penetrative fabric. Poles to S_2 in the northern half of the dome cluster in two point maxima that define the limbs of an open, upright, and gently NNW-plunging fold with a steeply dipping, NNW striking axial plane (Figure 9). Kink band and box fold orientations are non-systematic, likely due to local anisotropy and the pre-existing orientation of the folded layering.

5. Discussion of Condrey Mountain Schist Underplating Processes

Based on our structural data, the Lower Condrey unit records multiple prograde ductile deformation events (D_{1-3}). A pervasive foliation (S_2) developed across heterogeneous lithologies, including meter- to decameter-scale epidote blueschist and serpentinized ultramafic lenses. Despite multiple repeated mafic ± ultramafic lenses across the structural thickness (Figure 3), a third deformation event (D_3) only occurs proximal to the White and Scraggy Mountain mafic + ultramafic lenses. The Scraggy and White Mountain lenses also have strain localization in <10 m thick shear zones at their bases that do not occur with other mafic and/or ultramafic lenses.

Repeated mafic and/or ultramafic lenses (Figure 3) may represent: 1) the boundary of an underplated sliver with a ductile thrust at the base responsible for schist assembly or 2) material entrained in a thicker ductile

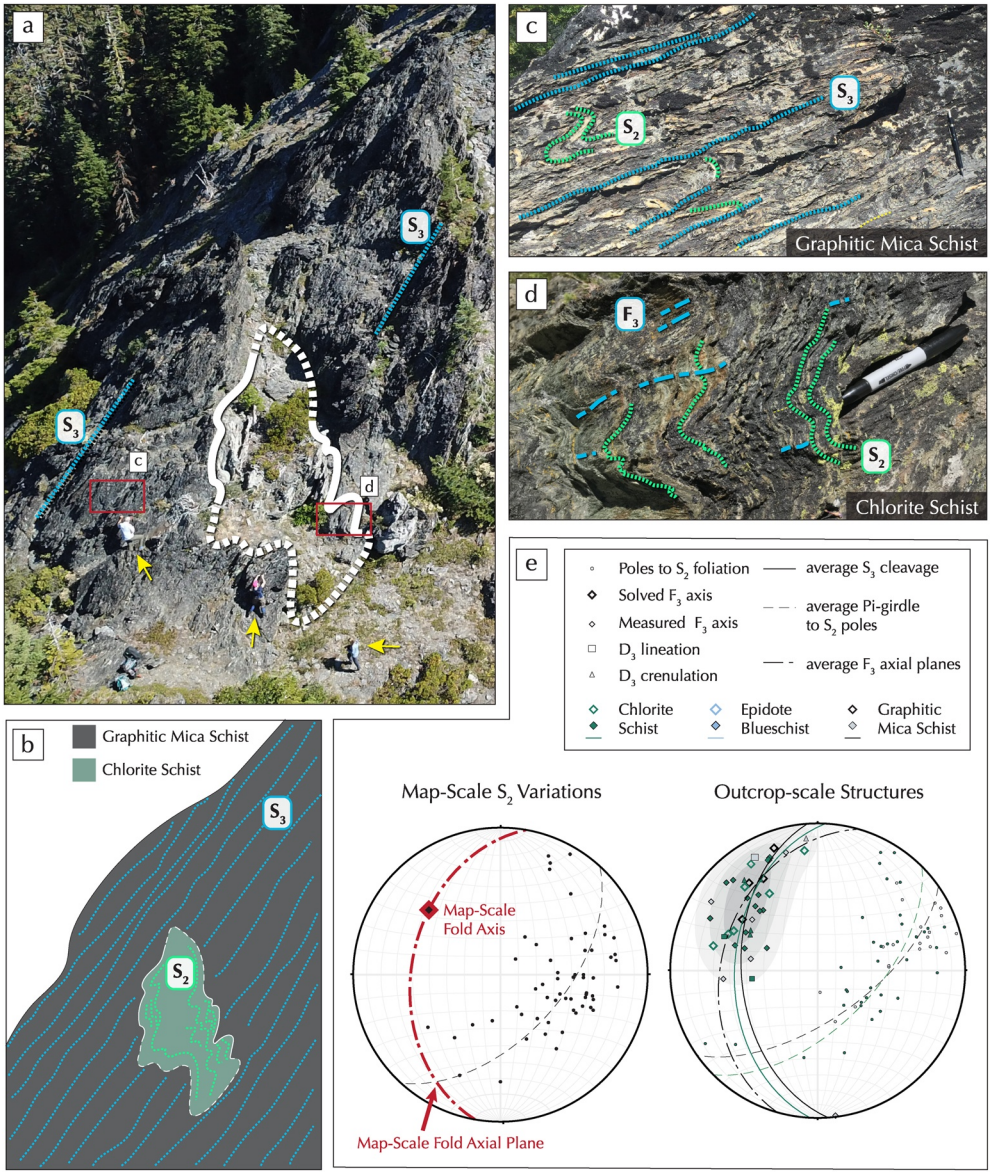

Figure 7. (a and b) Large-scale outcrop exposure of D_3 structures within chlorite and graphitic mica schist south of Scraggy Mountain (a) with a schematic sketch (b) of the key fabric elements and structures there. Red boxes indicate locations for photos (c and d). Yellow arrows in (a) mark people for scale. S_3 (blue dashed lines in all images) is a well-developed spaced cleavage in the graphitic mica schist (c) but is an incipient crenulation cleavage axial planar to F_3 in the chlorite schist (white outline in (a)). (c) In graphitic mica schist, S_2 (green dashed lines in all images) is only visible within microlithons of the strongly developed S_3 spaced cleavage, often defining F_3 microfolds. (d) S_2 in chlorite schist is folded with clear F_3 hinges, with a less well-developed S_3 axial planar crenulation cleavage. (e) Map-scale variations of S_2 (black circles) from Helper (1985) in the Scraggy Mountain region define a map-scale fold axial plane (red dashed line) and fold axis (red diamond) in the left stereonet. Outcrop-scale variation (right stereonet) in S_2 (circles) defines approximately parallel pi-girdles (dashed lines) and inferred fold axes (open diamonds) for both the graphitic mica schist (gray) and chlorite schist (green). Directly measured F_3 fold hinges (filled diamonds) are also approximately parallel, as are D_3 lineations (boxes) and crenulations (triangles). Gray contouring marks average orientations for all D_3 linear structures measured at outcrop (regardless of lithology). S_3 cleavage (solid lines) and axial planes (long-short dashed lines) in graphitic mica schist and chlorite schist are similarly parallel to each other and to the map-scale fold orientation.

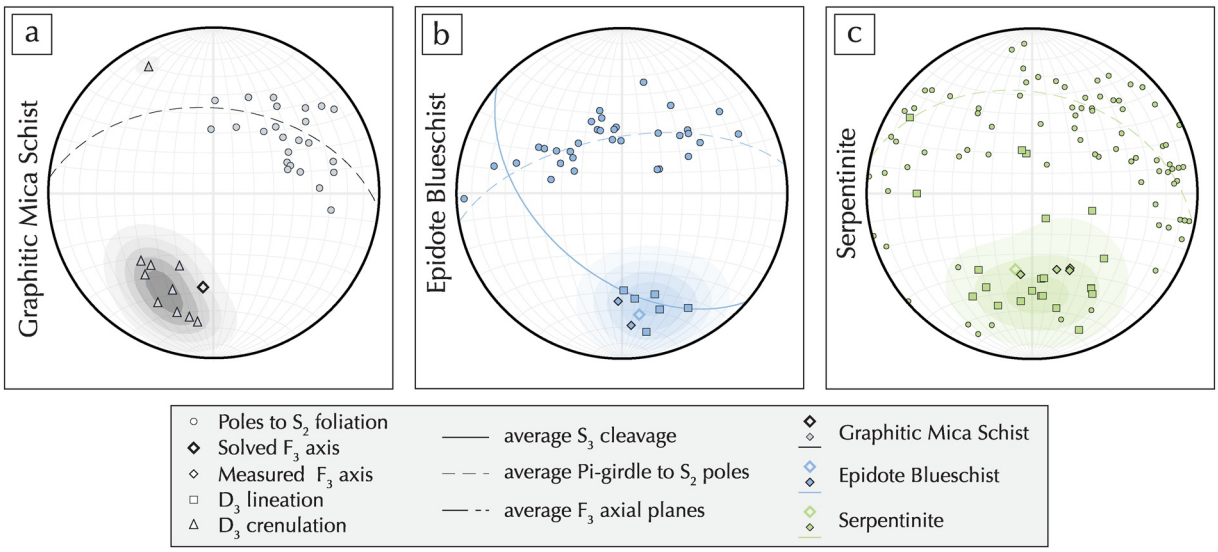

Figure 8. Stereonets for White Mountain D_3 structures in (a) graphitic mica schist, (b) epidote blueschist, and (c) serpentinite. White Mountain structures have similar orientations amongst heterogeneous lithologies. Directly measured F_3 fold axes (solid diamonds), calculated axes (open diamonds), lineations (squares) and crenulations (triangles) show slight variations amongst lithologies but are moderately S-plunging.

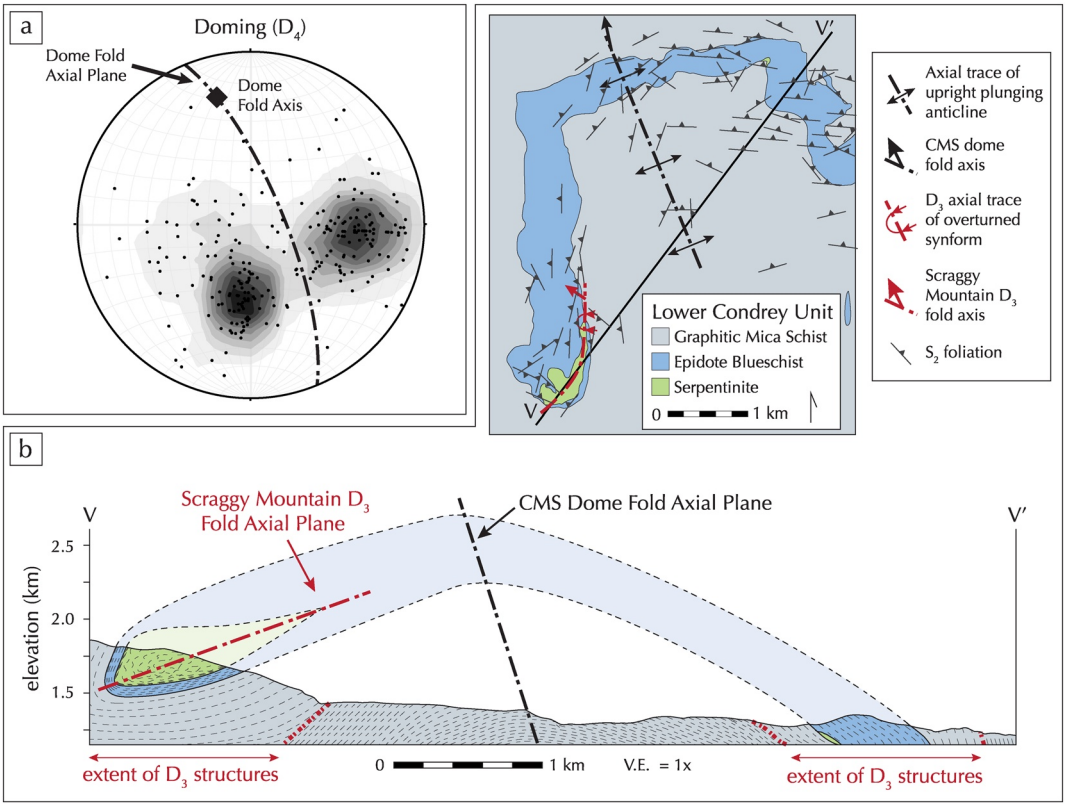

Figure 9. (a) Regional-scale variation in poles to S_2 (black dots) in the northern portion of the Condrey Mountain Schist dome defines two point maxima fit using standard stereographic analysis to determine the local dome fold axial plane (black dashed line) and axis (black diamond). (b) Cross-section along V-V′ showing the orientation of the S_2 foliation, the metaserpentinite-cored, reclined, isoclinal Scraggy Mountain D_3 synform, the geometry of the Condrey Mountain Schist dome in this area, and the areal extent of D_3 spaced cleavage and folds.

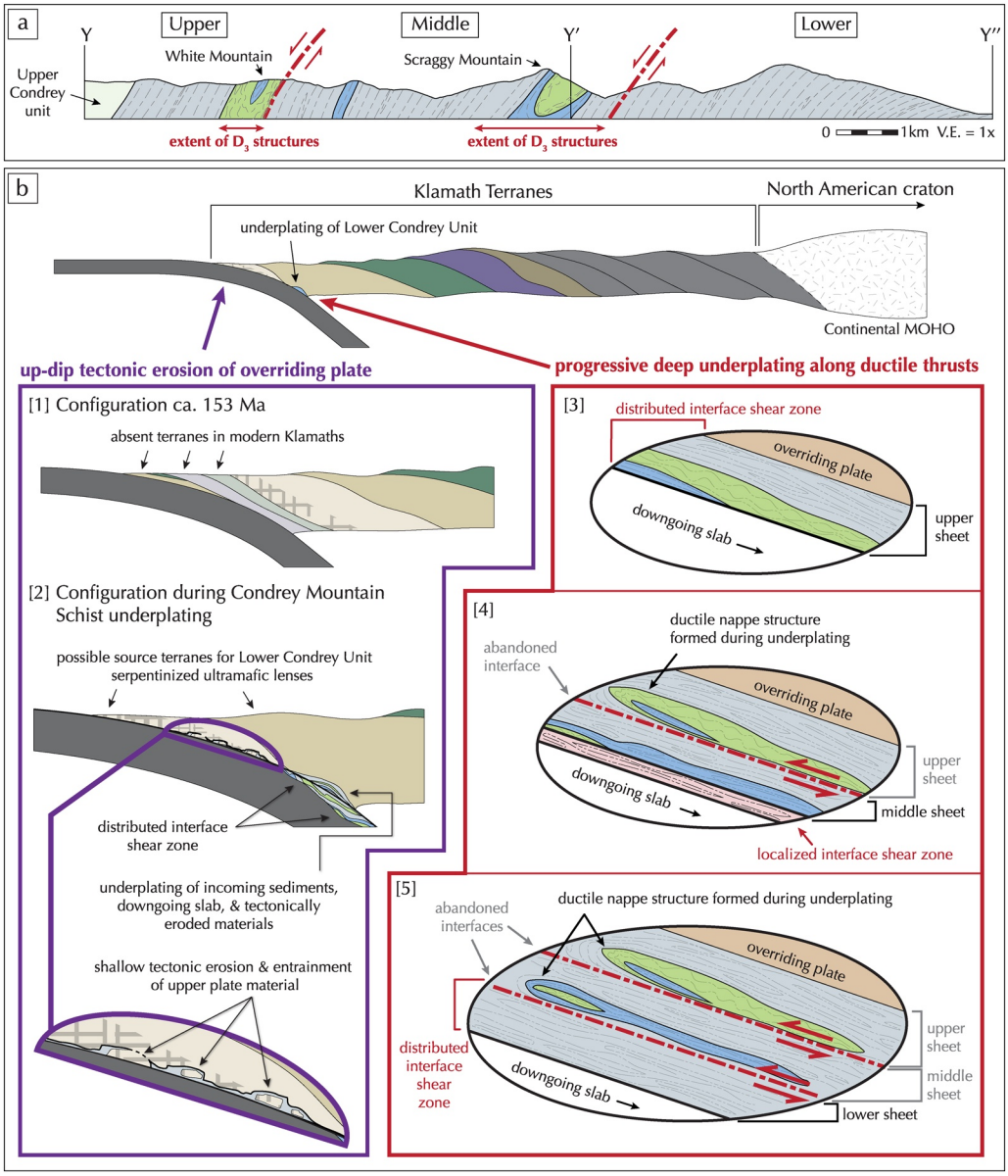

Figure 10. a) Cross-section of Lower Condrey unit along Y-Y′-Y″ (Figure 3) showing extent of D_3 structures, the location of inferred ductile thrusts (red dashed lines), and the broad division of the Lower Condrey unit into Upper, Middle, and Lower sheets that were progressively underplated. (b) Lower Condrey unit integrated tectonic history based on our combined geochemical, field, and structural data. Geochemical data suggest that ultramafic lenses and some mafic lenses were sourced through shallow tectonic erosion of the overriding plate (purple box), with incidental evidence of missing units ([1]) during Condrey Mountain Schist underplating ([2]). Progressive deep underplating with distributed strain ([3] and [5], red box) occurs in conjunction with periodic strain localization along ductile thrusts (red dashed lines and [4]) developing nappes in the hanging wall that are expressed as D_3 in the structural record ([4]).

shear zone. Because strain localization only occurs in conjunction with D_3 structures and is only locally developed proximal to the White and Scraggy Mountain lenses, we divide the Lower Condrey unit into underplated slices bounded by the occurrence of D_3 (upper, middle, and lower; Figure 10a). In this interpretation, $D_{1–2}$ structures relate to subduction interface shear zone deformation and entrainment of the packages between sheet boundaries, whereas D_3 and the strain localization relate to decoupling of the package from the downgoing slab and subsequent underplating. D_4 postdates the prograde ductile deformation and is likely related to Neogene doming (Mortimer & Coleman, 1985).

5.1. Evidence for Basal Erosion of the Forearc

The Lower Condrey unit is dominantly graphitic mica schist, derived from subduction of pelagic and hemipelagic sediment. In comparable modern margins, where the incoming sediment pile is thin (<0.5 km), the margins typically undergo subduction erosion, where material is plucked from the hanging wall and entrained along the subduction interface (e.g., Bassett et al., 2010; Clift & Hartley, 2007; Clift & Vannucchi, 2004; Von Huene & Scholl, 1991). Modern erosive subduction margins are defined by basal erosion of the forearc, where forearc wedge subsidence is used to infer subduction erosion rates (Clift & Vannucchi, 2004; Von Huene & Scholl, 1991). Behavior at depth (underplating or subduction of all material) is separate from shallow subduction erosion (e.g., the Hikurangi margin is classified as erosive despite seismic evidence for underplating near the mantle wedge corner, Bassett et al., 2010). Because subduction erosion is elusive in the rock record (cf., Agard et al., 2018), we use geochemical data and related contextual observations from the Condrey Mountain Schist to suggest that subduction erosion was operating along the Lower Condrey unit subduction margin (Figure 10) up-dip of final underplating depths, as evidenced by the following:

1. The high Cr# that characterizes relict chrome spinels of Lower Condrey unit metaserpentinites is consistent with forearc peridotite. Samples with anomalously low Mg# have brown halos around the chromite, suggesting late alteration that may modify mobile Mg (e.g., Middelburg et al., 1988). The samples without petrographic evidence for alteration have an average Mg# more characteristic of forearc peridotites. TiO_2 versus Al_2O_3 (both immobile; e.g., Middelburg et al., 1988) relationships for these same relict spinels fall outside of the abyssal peridotite fields or just within the overlap of forearc and abyssal fields, further supporting a forearc source (Figure 4b). Because the ultramafic geochemistry is inconsistent with a downgoing slab source, the Scraggy and White Mountain ultramafic lenses could have been sourced from: subaerial erosion resulting in olistoliths deposited in the trench or from subduction erosion of ultramafic rocks from the basal forearc. We favor the latter, noting the lack of other associated protoliths consistent with debris flow deposition (e.g., Festa et al., 2016) and the prevalence of uniformly fine-grained pelagic to hemipelagic schist. During Condrey Mountain Schist subduction, the overriding plate contains the Josephine Ophiolite, as well as ultramafic sources within the Rattlesnake Creek terrane, with chemistries that are comparable with Lower Condrey unit metaserpentinite geochemistry (Figure 4a and [1]–[2] in Figure 10b). Evidence of prograde D_{1-3} with limited retrograde ductile overprint (this study and Helper, 1986) suggests that serpentinite incorporation occurred up-dip of final underplating depths, whether entrained from the Klamath terranes in the forearc crust or from the forearc mantle. No serpentinized mantle is sandwiched between the Condrey Mountain Schist and the overlying terranes, suggesting that the Condrey Mountain Schist underplated shallower than the forearc mantle wedge corner ([2] in Figure 10b), making a serpentinized forearc mantle source unlikely.
2. The Klamath terranes provide indirect evidence for subduction erosion. Rifting of the Western Hayfork and Rattlesnake Creek terranes to form the Josephine Ophiolite basins should have produced a Western Hayfork/Rattlesnake Creek conjugate outboard of the Western Klamath terrane (Figure 2 and [1] in Figure 10b). The Western Klamath terrane, however, is in direct contact with the Franciscan Eastern Belt along much of its length (Figure 2a). Similarly, the active arc stepped outboard after Josephine backarc spreading initiated (Rogue Valley and Dry Butte subterranes), but is only locally preserved in the Oregon Klamaths (Figure 2a and [1] in Figure 10b) (e.g., Yule et al., 2006). Subduction erosion at other margins (e.g., Andes) has removed 250+ km of crust (Clift & Hartley, 2007). Subduction erosion up-dip of Condrey Mountain Schist underplating depths may have consumed these missing units in the Klamaths after collapse of the Josephine basins ([1]–[2] in Figure 10b).

Epidote blueschist trace element geochemistry is consistent with both downgoing slab and overriding plate sources (MORB and IAB, respectively). The Scraggy Mountain epidote blueschists have geochemical signatures similar to the Josephine Ophiolite and Rattlesnake Creek mafic components (Figure 4c) and suggest an IAB source (as they plot in IAB fields in Figure 4c and in the overlap of MORB and IAB fields in Figure 4d). Scraggy Mountain epidote blueschists are in contact with forearc-affinity serpentinized ultramafics and are interfolded with quartz-rich layers not observed elsewhere in the Lower Condrey unit (Figure 6a), permissibly consistent with arc-proximal deposits. Based on these observations, we interpret the Lower

Condrey unit Scraggy Mountain epidote blueschist lens as tectonically eroded from the basal forearc ([2] in Figure 10b).

In contrast, the Dry Lake epidote blueschists (Figure 3) are MORB-affinity with higher Zr concentrations on average than possible sources in the overriding Klamath terranes. They are also associated with deep ocean exhalites (Helper, 1986). Collectively, these results suggest that mafic lenses are incorporated into the schist through both shallow tectonic erosion up-dip of Condrey Mountain Schist underplating depths (arc-affinity, e.g., Scraggy Mountain) and entrainment and slicing of the downgoing slab (MORB-affinity, e.g., Dry Lake) (cf., Agard et al., 2018).

5.2. Assembly of the Lower Condrey Unit Through Coherent Underplating

The Lower Condrey unit has a complex history of prograde ductile deformation, but our detailed structural mapping characterized a phase of deformation (D_3) that overprints the pervasive foliation (S_2) and is spatially limited to large-scale rheological heterogeneities. The spatial distribution of D_3 fabric and structures separates the Lower Condrey unit into upper, middle, and lower sheets (Figure 10a). We interpret D_3 as a phase of progressive strain localization at the base of each previously underplated sheet driven by emplacement of the subsequent sheet.

Broad geometric kinematic consistency of D_3 structures amongst heterogeneous lithologies in the White and Scraggy Mountain lenses, separately, supports assembly of graphitic mica schist, mafic, and ultramafic protoliths prior to final emplacement. D_2 structures, where not overprinted by D_3, are similarly consistent across the graphitic mica schist and intercalated lenses of other materials. Combined with evidence for up-dip subduction erosion, we interpret the consistency of structures as evidence for a shared prograde deformation path and coherent emplacement amongst these heterogeneous lithologies.

All mafic and ultramafic lenses in the Condrey Mountain Schist are discontinuous along strike (Figure 3), suggesting original entrainment of lens-like slivers and/or boudinage after entrainment. White and Scraggy Mountain lenses, however, are cored by epidote blueschist and serpentinite lenses, respectively, with the primary lithology (serpentinite and epidote blueschist, respectively) fully encasing the lens at the core. The map geometry suggests infolding of the lenses at the core, and our preferred interpretation of the Scraggy Mountain structures is an overturned serpentinite-cored synform. By qualitatively unfolding the dome fold (Figure 9a) around the fold axis to restore S_2 surfaces to a moderate east dip, the Scraggy Mountain map-scale fold restores to an antiform with top-to-the-west sense of shear, suggesting a nappe related to prograde underplating in this east-dipping subduction zone. The map-scale and outcrop-scale D_3 orientations are comparable, suggesting that outcrop-scale structures are parasitic. We propose that outcrop-scale and coeval map-scale F_3 formed by ductile entrainment of the hanging wall (middle sheet) during lower sheet emplacement ([5] in Figure 10b). Similarly, we interpret White Mountain as a ductile nappe cored with an epidote blueschist lens formed during initial underplating of the middle sheet ([4] in Figure 10b). With these interpretations, D_3 represents strain localization along ductile thrusts at White and Scraggy Mountains responsible for progressive and subsequent underplating of the middle and lower sheets, respectively.

6. Implications

6.1. Subduction Interface Shear Zone Rheology and Underplating Processes

Subduction interface rheology recorded in the Lower Condrey unit was dominated by two endmembers that appear to have alternated during the tectonic history: 1) distributed viscous deformation across dominantly metasedimentary packages, and 2) localized viscous deformation along serpentinized margins of lensoidal ultramafic bodies, discussed further below.

1. *Distributed, sediment-dominated shear zone*. Prograde deformation structures are consistent within the Lower Condrey unit thrust-bounded sheets, with no field evidence of strain localization within the 2+ km thicknesses. Alternating compositional domains defining S_{1-3} in the graphitic mica schist are consistent with deformation by pressure solution, a linear-viscous mechanism (e.g., Den Brok, 1998; Passchier & Trouw, 2005). Meter- to decameter-scale mafic and ultramafic lenses (Figure 3) within this dominantly pelagic to hemipelagic metasedimentary shear zone have comparable rheology and do not perturb

distributed deformation. Evidence from other field areas similarly supports a low rheologic contrast between epidote blueschists and mica schists (e.g., Kotowski & Behr, 2019; Tulley et al., 2020).

2. *Localized serpentinite shear zone*. Progressive strain localization in km-scale serpentinite and epidote blueschist lenses to zones of <10 m at the base (Figure 5d) suggests that the margins of these mafic + ultramafic lenses served as rheologic weaknesses that facilitated localized strain. Although field evidence suggests that small serpentinite lenses are rheologically homogeneous, the large serpentinite + epidote blueschist lenses are rheologically heterogeneous. The larger lenses may not have been fully serpentinized during subduction (e.g., serpentinite rimmed and peridotite cored). Fully serpentinized small lenses deformed coherently with the surrounding graphitic mica schist, whereas juxtaposition of relatively weak serpentinite at the margins of strong peridotite allowed for strain localization. Timing of serpentinization is unconstrained, but the presence of antigorite serpentinite suggests it was ongoing near peak metamorphic conditions.

We interpret the evidence for distributed deformation in sedimentary protoliths to record the distribution of strain on the deep interface between underplating episodes. The structural thickness of each sheet (2+ km) is much greater than the incoming sediment thickness in modern erosive margins (Clift & Vannucchi, 2004). To accumulate the observed structural thickness, individual thrust-bounded sheets must have grown from progressively underplated thin packages (<0.5 km) of graphitic mica schist and decameter-scale intercalated lenses of mafic and ultramafic material. Discrete fabrics and thrusts associated with such growth between the major ductile thrusts at White and Scraggy Mountains are, however, lacking, suggesting continuous entrainment that masks any definitive earlier record of growth ([3] and [5] in Figure 10b). In contrast to a subduction interface that steps successively and discretely downward, rheologic homogeneity between previously underplated and actively underplating sediments resulted in strong coupling and a progressively widening shear zone up to 2+ km thick.

The process of deep underplating that we infer from the Lower Condrey unit exhibits some similarities and some differences compared to interpretations of other exhumed terranes. All models for deep underplating require strain localization to a weak zone that allows for decoupling from the downgoing slab followed by attachment to the overriding plate (e.g., Agard et al., 2018). What constitutes the weak zones that allow for decoupling appears to vary for different subduction depths and different localities, but can include weak and/or overpressurized sediments (e.g., Byrne & Fisher, 1990; Kimura & Ludden, 1995; Meneghini et al., 2009; Plunder et al., 2012), altered oceanic crust (e.g., Kameda et al., 2017; Kimura & Ludden, 1995), or serpentinized mantle (e.g., Angiboust et al., 2011; Cluzel et al., 2001; Hilairet & Reynard, 2009; Ruh et al., 2015; Vogt & Gerya, 2014). In most subduction complexes where weakening is associated with serpentinization, the source of ultramafic material is interpreted to be the downgoing slab mantle (Angiboust et al., 2011; Cluzel et al., 2001). Modeling further supports the importance of strain localization in serpentinite in the downgoing slab mantle as a decoupling mechanism (Ruh et al., 2015; Vogt & Gerya, 2014). Our results support the general interpretation of decoupling via serpentinite weakening. The margins of km-scale mafic and ultramafic lenses in the Lower Condrey unit served as weak zones along which strain could localize, decoupling the previously entrained sediment packages from the downgoing slab ([4] in Figure 10b). One key difference from interpretations from other subduction complexes, however, is that we interpret the serpentinite in the Lower Condrey unit to have been derived from the overriding plate via up-dip basal erosion, rather than from the downgoing slab. We suggest that subduction and entrainment of these upper plate ultramafic lenses temporarily altered the interface rheology through serpentinization farther down-dip, allowing for strain localization below the previously entrained packages and subsequent underplating at depth.

We further quantified the importance of shear zone lithology using a force-balance derived by Bialas et al. (2011) (Text S1). Subduction versus underplating/return flow depends on the balance between 1) package thickness and density contrast (buoyancy force, Figure 11a) and 2) the strength and thickness of the basal shear zone separating the package and the downgoing slab (drag force, Figure 11a). A strong basal shear zone (i.e., high viscosity) will couple the package to the downgoing slab, and the package will subduct (blue field, Figure 11b). Underplating or return flow requires a weaker basal shear zone. For a 4 km thick package of sediments plus minor mafic and ultramafic components (e.g., the Lower Condrey unit middle sheet), strain localization into a sediment-dominated basal shear zone results in subduction because the

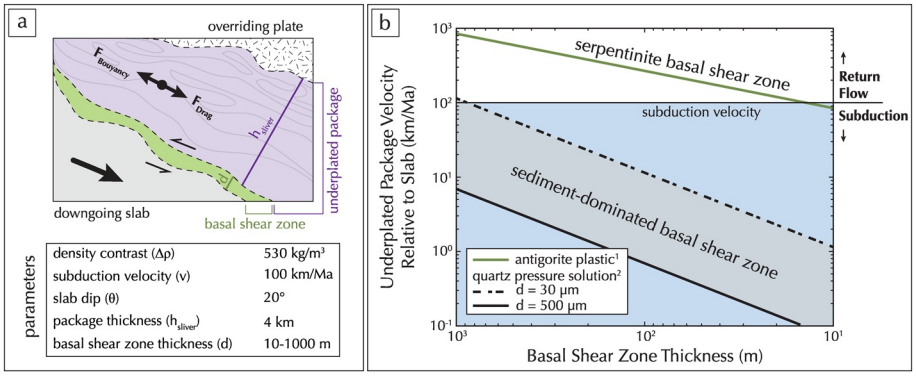

Figure 11. (a) Schematic and parameters for force-balance calculations using the derivation in Bialas et al. (2011) showing assumed configuration of the underplated package and basal shear zone. (b) Lines plot the relative velocity of a 4 km thick package of sediment plus minor mafic and ultramafic components (e.g., the Lower Condrey unit Middle sheet) for a given basal shear zone thickness. When $v_{relative} = v_{subduction}$, the package has underplated. If $v_{relative} < v_{subduction}$, the drag force exceeds the buoyancy, and the package will subduct (blue field). If $v_{relative} > v_{subduction}$, the buoyancy force is greater, and the package undergoes return flow. Strain localization to a sediment-dominated basal shear zone (gray field between solid and dashed black lines) results in strong coupling to the slab and subduction of the package. A serpentine basal shear zone (green line) is weak enough to allow for underplating and/or return flow during strain localization. Basal shear zone viscosity was calculated with an antigorite plastic flow law (Amiguet et al., 2014)[1] consistent with observed microstructures and a quartz pressure solution flow law (stress corrosion microcracking, Den Brok, 1998),[2] which is consistent with observed microstructures and predicted strain rates (comparison to other flow laws from Cox and Paterson (1991) and Rutter (1976) detailed in Text S1 and Figure S1).

predicted viscosities (pressure solution flow law from Den Brok, 1998) (Text S1 and Figure S1) are too high to decouple from the downgoing slab (solid and dashed black lines, Figure 11b). A serpentine basal shear zone, however, will result in underplating or return flow due to low viscosities (flow law from Amiguet et al., 2014) (green line, Figure 11b). These calculations support our field observations that serpentine plays an important role in underplating.

Interface lithologies further govern the geophysical expression of the subduction interface. The Lower Condrey unit distributed, sediment-dominated interface shear zone has comparable thicknesses to the LVZ observed in modern subduction zones (e.g., Bostock, 2013), consistent with inferences that the LVZ may represent a ductile interface shear zone incorporating heterogenous lithologies (Bostock, 2013; Calvert et al., 2020; Delph et al., 2018; Nedimović et al., 2003). Because LVZ velocities are typically attributed to high pore fluid pressures (Abers et al., 2009; Audet & Kim, 2016; Bostock, 2013; Calvert et al., 2011, 2020; Hansen et al., 2012) as opposed to lithology alone (Bostock, 2013), further research is needed to determine if Lower Condrey unit lithologies would have comparable seismic velocities during subduction and underplating. In addition, modern LVZs are collocated with transient seismic and aseismic slip events (Audet & Kim, 2016) that have been attributed to either slip on a heterogeneous frictional interface (e.g., Chestler & Creager, 2017; Y. Ito et al., 2007; Lay et al., 2012; Luo & Ampuero, 2018; Shelly et al., 2006) or brittle failure of blocks within a distributed ductile interface shear zone (e.g., Beall et al., 2019; Behr et al., 2018; Hayman & Lavier, 2014; Kotowski & Behr, 2019; Tarling et al., 2019; Ujiie et al., 2018). This evidence of a distributed interface further supports the later, and these thickness constraints can be compared to the estimated width of transient slip event producing zones in modern margins.

6.2. Long-Term Sediment Storage in Erosive Subduction Margins

Continental mass and carbon budgets typically split modern subduction margins into "accretionary" and "erosive" to better define material supply and reservoirs (e.g., Clift & Hartley, 2007; Clift & Vannucchi, 2004; Von Huene & Scholl, 1991). Accretionary margins are those that exhibit thick incoming sediment packages and undergo frontal accretion and significant underplating at the base of the accretionary wedge. Erosive margins, on the other hand, have thin to nonexistent incoming sediment packages, leading to tectonic erosion of the overriding plate (Clift et al., 2009; Von Huene & Scholl, 1991). Net negative fluxes for carbon and continental mass budgets include all material subducted past the accretionary wedge (e.g., not preserved

through frontal accretion or shallow underplating) and all tectonically eroded material (Clift et al., 2009; Von Huene & Scholl, 1991). Erosive margins in particular are calculated to supply 60% of the continental material and 35% of the total carbon subducted to the upper mantle (Clift, 2017; Clift et al., 2009).

A key assumption in calculating the high negative fluxes for margins that undergo subduction erosion is that *underplating does not occur at any depth along the interface*. We have presented evidence here, however, of a fossil subduction margin that appears to have been erosive at depths <25–35 km, but that underwent progressive underplating at deeper levels. Preservation of the Lower Condrey unit in the rock record further indicates that underplating in this shallowly erosive margin was permanent; that is, the underplated material was not temporarily "parked" at depth and later eroded and subducted to the Earth's interior.

Although difficult without precise timing constraints, we can place some bounds on the percentage of underplated material represented by the Lower Condrey unit relative to the amount of sediment supplied to the trench. Using previously published gravity data (Jachens & Elder, 1983) and map exposure, we estimate that the cross-sectional area of the Lower Condrey unit is ca. 45 km^2. The timing of Lower Condrey unit underplating is bracketed to a maximum of ca. 32 m.y. by 1) emplacement of the top of the Upper Condrey unit at 155 Ma (Saleeby & Harper, 1993), and 2) outboard onset of Franciscan underplating at 123 Ma (Dumitru et al., 2010). We estimate sediment supply rates by averaging incoming sediment thicknesses for modern erosive subduction margins (Clift et al., 2009), correcting for porosity (Clift & Vannucchi, 2004), and integrating over the range of reconstructed Farallon plate velocities at Klamath latitudes (Engebretson et al., 1985). Combining the estimated sediment supply with the maximum emplacement time, the Lower Condrey unit is calculated to represent the underplated record of ca. 10% of the incoming sediment. As Mesozoic sedimentation rates were likely lower than modern (Clift, 2017) and the timeframe is a maximum, these values represent absolute lower bounds. Additionally, the assumed Lower Condrey unit underplating duration does not account for the time needed to assemble the Upper Condrey unit structural thickness, suggesting that the actual duration was likely shorter. Detailed metamorphic ages on the Franciscan Eastern Belt, a subduction complex outboard of the Condrey Mountain Schist with comparable structural thicknesses and protoliths, place underplating duration at 10 m.y. (Dumitru et al., 2010). If we assume a similar duration for the Lower Condrey unit, underplating percentages range from 20% to 60% of the incoming sediment.

The Condrey Mountain Schist example of deep underplating in an erosive margin environment is consistent with emerging evidence for coeval subduction erosion and underplating in fossil and modern subduction environments (Angiboust et al., 2018; Bassett et al., 2010; Clift & Hartley, 2007; Cluzel et al., 2001; Eberhart-Phillips & Chadwick, 2002). Seismic imaging of the erosive northern Hikurangi margin, for example, revealed 10+ km of sediments and tectonically eroded materials underplated at the mantle wedge corner (Bassett et al., 2010; Eberhart-Phillips & Chadwick, 2002). Clift and Hartley (2007) inferred similar underplating from terrace uplift along the Andean margin and argued for significant (>80%) underplating of incoming material. Previous estimates of underplating percentages in Hikurangi (30%–60%, Bassett et al., 2010, percent calculated from Clift et al. (2009) sediment supply and estimate of tectonically eroded material) and the Andes (80%, Clift & Hartley, 2007) are consistent with the upper bounds of our Lower Condrey unit estimate. Previous quantification of the percent of subducted pelitic sediment later exhumed in a comparable, but non-erosive, fossil subduction margin (Schistes Lustrés) is similarly consistent at 50% (Agard et al., 2009). Improved emplacement timing for the Lower Condrey unit, which will bracket both the underplating duration and plate velocities, can better constrain these values. Further analysis of other modern and fossil subduction complexes is needed to understand the ubiquitousness of underplating in erosive margins and the possible impact on mass and volatile recycling estimates in modern subduction zones.

7. Conclusions

The Condrey Mountain Schist, northern California and southern Oregon, records coherent underplating at 25–35 km depth coeval with up-dip subduction erosion of the overriding plate that sourced serpentinized ultramafic and some mafic protoliths. Two major ductile thrusts along km-scale mafic and ultramafic lenses divide the Lower Condrey unit into three thrust sheets. Progressive underplating and entrainment of dominantly sedimentary protoliths resulted in a widening shear zone. Periodic strain localization to the ductile

thrusts facilitated underplating by allowing for decoupling from the downgoing slab. This rock record evidence provides constraints on subduction interface shear zone rheology, as well as mass and volatile recycling, in modern subduction zones. The subduction interface in the Lower Condrey unit was characterized by distributed viscous deformation across 2+ km of predominantly sedimentary protoliths despite being a sediment-poor margin, possibly consistent with the LVZ and transient seismic and aseismic slip events observed in modern subduction zones. Current mass and volatile budgets are well-balanced but assume no underplating in erosive margins. The Lower Condrey unit and several modern erosive margins, however, record significant preservation of incoming material. Better characterization of underplating percentages in erosive margins is crucial to accurately predict the net flux of mass and volatiles to the Earth's interior.

Data Availability Statement

Legacy data sets for this research are included in this paper: C. G. Barnes et al. (1995). All data collected by the authors (including structural data reconstructed from Helper [1985]) are available from the ETH Research Collection data repository at https://doi.org/10.3929/ethz-b-000456096. Data sources are listed in Sections 3.1 and 4.

Acknowledgments
This work was supported by a National Science Foundation (NSF) CAREER Grant (EAR-1555346) and a European Research Council (ERC) Starting Grant (947659) awarded to W. M. Behr. We are grateful to Philippe Agard and Donald Fisher for their insightful reviews that strengthened this manuscript. We also thank Julien Cornet for assisting with data collection on the ETH Zurich Electron Probe Microanalyser and Ranger Donna Mickley and the staff at the Star Ranger Station in the Rogue River-Siskyou National Forest for their support of our fieldwork.

References

Abers, G. A., MacKenzie, L. S., Rondenay, S., Zhang, Z., Wech, A. G., & Creager, K. C. (2009). Imaging the source region of Cascadia tremor and intermediate-depth earthquakes. *Geology*, *37*(12), 1119–1122.

Agard, P., Plunder, A., Angiboust, S., Bonnet, G., & Ruh, J. (2018). The subduction plate interface: Rock record and mechanical coupling (from long to short timescales). *Lithos*, *320–321*, 537–566.

Agard, P., Yamato, P., Jolivet, L., & Burov, E. (2009). Exhumation of oceanic blueschists and eclogites in subduction zones: Timing and mechanisms. *Earth-Science Reviews*, *92*(1–2), 53–79.

Agurto, H., Rietbrock, A., Ryder, I., & Miller, M. (2012). Seismic-afterslip characterization of the 2010 Mw 8.8 Maule, Chile, earthquake based on moment tensor inversion. *Geophysical Research Letters*, *39*, L20303. https://doi.org/10.1029/2012GL053434

Allmendinger, R. W., Cardozo, N., & Fisher, D. M. (2011). *Structural geology algorithms: Vectors and tensors*. Cambridge University Press.

Amiguet, E., Van De Moortèle, B., Cordier, P., Hilairet, N., & Reynard, B. (2014). Deformation mechanisms and rheology of serpentines in experiments and in nature. *Journal of Geophysical Research: Solid Earth*, *119*(6), 4640–4655. https://doi.org/10.1002/2013JB010791

Angiboust, S., Agard, P., Raimbourg, H., Yamato, P., & Huet, B. (2011). Subduction interface processes recorded by eclogite-facies shear zones (Monviso, W. Alps). *Lithos*, *127*(1–2), 222–238.

Angiboust, S., Cambeses, A., Hyppolito, T., Glodny, J., Monié, P., Calderón, M., & Juliani, C. (2018). A 100-my-long window onto mass-flow processes in the Patagonian Mesozoic subduction zone (Diego de Almagro Island, Chile). *Geological Society of America Bulletin*, *130*(9–10), 1439–1456.

Aoki, K., Kitajima, K., Masago, H., Nishizawa, M., Terabayashi, M., Omori, S., et al. (2009). Metamorphic P–T–time history of the Sanbagawa belt in central Shikoku, Japan and implications for retrograde metamorphism during exhumation. *Lithos*, *113*(3–4), 393–407.

Audet, P., & Kim, Y. (2016). Teleseismic constraints on the geological environment of deep episodic tremor and slow earthquakes in subduction zone forearcs: A review. *Tectonophysics*, *670*, 1–15.

Audet, P., & Schaeffer, A. J. (2018). Fluid pressure and shear zone development over the locked to slow slip region in Cascadia. *Science Advances*, *4*(3), eaar2982.

Barnes, C. G., & Barnes, M. A. (2020). The western Hayfork terrane: Remnants of the Middle Jurassic arc in the Klamath Mountain province, California and Oregon. *Geosphere*, *16*(4), 1058–1081.

Barnes, C. G., Donato, M. M., Barnes, M. A., Yule, J. D., Hacker, B. R., & Helper, M. A. (1995). *Geochemical compositions of metavolcanic and metasedimentary rocks, western Jurassic and western Paleozoic and Triassic belts, Klamath Mountains, Oregon and California*. USGS Open File Report, 95–227-A, 1–64.

Barnes, C. G., Snoke, A. W., Harper, G. D., Frost, C. D., McFadden, R. R., Bushey, J. C., & Barnes, M. A. (2006). Arc plutonism following regional thrusting: Petrology and geochemistry of syn- and post-Nevadan plutons in the Siskiyou Mountains, Klamath Mountains province, California. *Geological Society of America Special Paper*, *410*, 357–376.

Barnes, J. D., Eldam, R., Lee, C.-T. A., Errico, J. C., Loewy, S., & Cisneros, M. (2013). Petrogenesis of serpentinites from the Franciscan Complex, western California, USA. *Lithos*, *178*, 143–157.

Bassett, D., Sutherland, R., Henrys, S., Stern, T., Scherwath, M., Benson, A., et al. (2010). Three-dimensional velocity structure of the northern Hikurangi margin, Raukumara, New Zealand: Implications for the growth of continental crust by subduction erosion and tectonic underplating. *Geochemistry, Geophysics, Geosystems*, *11*(10), 1–24. https://doi.org/10.1029/2010GC003137

Beall, A., Fagereng, Å., & Ellis, S. (2019). Strength of strained two-phase mixtures: Application to rapid creep and stress amplification in subduction zone mélange. *Geophysical Research Letters*, *46*(1), 169–178. https://doi.org/10.1029/2018GL081252

Behr, W. M., & Becker, T. W. (2018). Sediment control on subduction plate speeds. *Earth and Planetary Science Letters*, *502*, 166–173.

Behr, W. M., & Burgmann, R. (2020). What's down there? The structures, materials and environment of deep-seated tremor and slip. *Philosophical Transactions of Royal Society A*, *379*, 20200218. https://doi.org/10.1098/rsta.2020.0218

Behr, W. M., Kotowski, A. J., & Ashley, K. T. (2018). Dehydration-induced rheological heterogeneity and the deep tremor source in warm subduction zones. *Geology*, *46*(5), 475–478.

Behr, W. M., & Platt, J. P. (2013). Rheological evolution of a Mediterranean subduction complex. *Journal of Structural Geology*, *54*, 136–155.

Beroza, G. C., & Ide, S. (2009). Deep tremors and slow quakes. *Science*, *324*(5930), 1025–1026.

Bialas, R. W., Funiciello, F., & Faccenna, C. (2011). Subduction and exhumation of continental crust: Insights from laboratory models. *Geophysical Journal International*, *184*(1), 43–64.

Bostock, M. (2013). The Moho in subduction zones. *Tectonophysics*, *609*, 547–557.

Byrne, T., & Fisher, D. (1990). Evidence for a weak and overpressured decollement beneath sediment-dominated accretionary prisms. *Journal of Geophysical Research*, *95*(B6), 9081–9097.
Calvert, A. J., Bostock, M. G., Savard, G., & Unsworth, M. J. (2020). Cascadia low frequency earthquakes at the base of an overpressured subduction shear zone. *Nature Communications*, *11*(1), 1–10.
Calvert, A. J., Preston, L. A., & Farahbod, A. M. (2011). Sedimentary underplating at the Cascadia mantle-wedge corner revealed by seismic imaging. *Nature Geoscience*, *4*(8), 545–548.
Cardozo, N., & Allmendinger, R. W. (2013). Spherical projections with OSXStereonet. *Computers & Geosciences*, *51*, 193–205.
Chestler, S. R., & Creager, K. C. (2017). Evidence for a scale-limited low-frequency earthquake source process. *Journal of Geophysical Research: Solid Earth*, *122*(4), 3099–3114. http://dx.doi.org/10.1002/2016jb013717
Clift, P. (2017). A revised budget for Cenozoic sedimentary carbon subduction. *Reviews of Geophysics*, *55*(1), 97–125. https://doi.org/10.1002/2016RG000531
Clift, P., & Hartley, A. J. (2007). Slow rates of subduction erosion and coastal underplating along the Andean margin of Chile and Peru. *Geology*, *35*(6), 503–506.
Clift, P., & Vannucchi, P. (2004). Controls on tectonic accretion versus erosion in subduction zones: Implications for the origin and recycling of the continental crust. *Reviews of Geophysics*, *42*, RG2001. https://doi.org/10.1029/2003RG000127
Clift, P., Vannucchi, P., & Morgan, J. P. (2009). Crustal redistribution, crust-mantle recycling and Phanerozoic evolution of the continental crust. *Earth-Science Reviews*, *97*(1–4), 80–104.
Cloos, M., & Schreve, R. R. (1988). Subduction-channel model of prism accretion, melange formation, sediment subduction, and subduction erosion at convergent plate margins: 1. Background and description. *Pure and Applied Geophysics*, *128*(3–4), 455–500.
Cluzel, D., Aitchison, J. C., & Picard, C. (2001). Tectonic accretion and underplating of mafic terranes in the Late Eocene intraoceanic fore-arc of New Caledonia (Southwest Pacific): Geodynamic implications. *Tectonophysics*, *340*(1–2), 23–59.
Coleman, R., & Helper, M. (1983). The significance of the Condrey Mountain Dome in the evolution of the Klamath Mountains. *California and Oregon: Geological Society of America Abstracts with Programs*, *15*(5), 294.
Cox, S., & Paterson, M. (1991). Experimental dissolution-precipitation creep in quartz aggregates at high temperatures. *Geophysical Research Letters*, *18*(8), 1401–1404.
Davis, D., Suppe, J., & Dahlen, F. (1983). Mechanics of fold-and-thrust belts and accretionary wedges. *Journal of Geophysical Research*, *88*(B2), 1153–1172.
Delph, J. R., Levander, A., & Niu, F. (2018). Fluid controls on the heterogeneous seismic characteristics of the Cascadia margin. *Geophysical Research Letters*, *45*(20), 11021–11029. https://doi.org/10.1029/2018GL079518
Den Brok, S. (1998). Effect of microcracking on pressure-solution strain rate: The Gratz grain-boundary model. *Geology*, *26*(10), 915–918.
Dickinson, W. R. (2004). Evolution of the North American Cordillera. *Annual Review of Earth and Planetary Sciences*, *32*, 13–45.
Donato, M., Coleman, R., & Kays, M. (1980). Geology of the Condrey Mountain Schist, northern Klamath Mountains. *California and Oregon: Oregon Geology*, *42*(2), 125–129.
Dumitru, T. A., Wakabayashi, J., Wright, J. E., & Wooden, J. L. (2010). Early Cretaceous transition from nonaccretionary behavior to strongly accretionary behavior within the Franciscan subduction complex. *Tectonics*, *29*, 1–24. https://doi.org/10.1029/2009TC002542
Eberhart-Phillips, D., & Chadwick, M. (2002). Three-dimensional attenuation model of the shallow Hikurangi subduction zone in the Raukumara Peninsula, New Zealand. *Journal of Geophysical Research*, *107*(B2), ESE-3. https://doi.org/10.1029/2000JB000046
Engebretson, D. C., Cox, A., & Gordon, R. G. (1985). Relative motions between oceanic and continental plates in the Pacific Basin. *Geological Society of America Special Paper*, *206*, 1–58.
Ernst, W. G. (2015). Franciscan geologic history constrained by tectonic/olistostromal high-grade metamafic blocks in the iconic California Mesozoic-Cenozoic accretionary complex. *American Mineralogist*, *100*(1), 6–13.
Evans, B. W. (1990). Phase relations of epidote-blueschists. *Lithos*, *25*(1–3), 3–23.
Fagereng, A., & Ellis, S. (2009). On factors controlling the depth of interseismic coupling on the Hikurangi subduction interface, New Zealand. *Earth and Planetary Science Letters*, *278*(1–2), 120–130.
Fagereng, A., & Sibson, R. H. (2010). Melange rheology and seismic style. *Geology*, *38*(8), 751–754.
Festa, A., Ogata, K., Pini, G. A., Dilek, Y., & Alonso, J. L. (2016). Origin and significance of olistostromes in the evolution of orogenic belts: A global synthesis. *Gondwana Research*, *39*, 180–203.
Frost, C. D., Barnes, C. G., & Snoke, A. W. (2006). Nd and Sr isotopic data from argillaceous rocks of the Galice Formation and Rattlesnake Creek terrane, Klamath Mountains: Evidence for the input of Precambrian sources. *Geological Society of America Special Paper*, *410*, 103–120.
Garlick, S. R., Medaris, L. G., Jr., Snoke, A. W., Schwartz, J. J., & Swapp, S. M. (2009). Granulite-to amphibolite-facies metamorphism and penetrative deformation in a disrupted ophiolite, Klamath Mountains, California: A deep view into the basement of an accreted oceanic arc. *Geological Society of America Special Paper*, *456*, 151–186.
Graham, C. M., Tareen, J. A., McMillan, P. F., & Lowe, B. M. (1992). An experimental and thermodynamic study of cymrite and celsian stability in the system BaO-Al_2O_3-SiO_2-H_2O. *European Journal of Mineralogy*, *4*(2), 251–269.
Graveleau, F., Malavieille, J., & Dominguez, S. (2012). Experimental modelling of orogenic wedges: A review. *Tectonophysics*, *538*, 1–66.
Gray, G. G. (1986). Native terranes of the central Klamath Mountains, California. *Tectonics*, *5*(7), 1043–1054.
Hacker, B. R., Donato, M. M., Barnes, C. G., McWilliams, M., & Ernst, W. (1995). Timescales of orogeny: Jurassic construction of the Klamath Mountains. *Tectonics*, *14*(3), 677–703.
Hamilton, W. (1969). Mesozoic California and the underflow of Pacific mantle. *Geological Society of America Bulletin*, *80*(12), 2409–2430.
Hansen, R. T., Bostock, M. G., & Christensen, N. I. (2012). Nature of the low velocity zone in Cascadia from receiver function waveform inversion. *Earth and Planetary Science Letters*, *337*, 25–38.
Harper, G. D., Saleeby, J. B., & Heizler, M. (1994). Formation and emplacement of the Josephine ophiolite and the Nevadan orogeny in the Klamath Mountains, California-Oregon: U/Pb zircon and $^{40}Ar/^{39}Ar$ geochronology. *Journal of Geophysical Research*, *99*(B3), 4293–4321.
Hayman, N. W., & Lavier, L. L. (2014). The geologic record of deep episodic tremor and slip. *Geology*, *42*(3), 195–198. http://dx.doi.org/10.1130/g34990.1
Helper, M. (1985). *Structural, metamorphic and geochronologic constrains on the origin of the Condrey Mountain Schist, north central Klamath Mountains, northern California* (Unpublished doctoral dissertation). University of Texas at Austin.
Helper, M. (1986). Deformation and high P/T metamorphism in the central part of the Condrey Mountain window, north-central Klamath Mountains, California and Oregon. *GSA Memoir*, *164*, 125–142.
Hilairet, N., & Reynard, B. (2009). Stability and dynamics of serpentinite layer in subduction zone. *Tectonophysics*, *465*(1–4), 24–29.

Hopson, C. A., Mattinson, J. M., Pessagno, E. A., & Luyendyk, B. P. (2008). California Coast Range ophiolite: Composite Middle and Late Jurassic oceanic lithosphere. *Geological Society of America Special Paper*, *438*, 1–102.
Ito, T., Kojima, Y., Kodaira, S., Sato, H., Kaneda, Y., Iwasaki, T., & Ikawa, T. (2009). Crustal structure of southwest Japan, revealed by the integrated seismic experiment Southwest Japan 2002. *Tectonophysics*, *472*(1–4), 124–134.
Ito, Y., Obara, K., Shiomi, K., Sekine, S., & Hirose, H. (2007). Slow earthquakes coincident with episodic tremors and slow slip events. *Science*, *315*(5811), 503–506.
Jachens, R. C., & Elder, W. P. (1983). *Aeromagnetic map and interpretation of geophysical data from the Condrey Mountain roadless area*. Siskiyou County, California: USGS Miscellaneous Field Studies Map 1540-B.
Jarrard, R. D. (2003). Subduction fluxes of water, carbon dioxide, chlorine, and potassium. *Geochemistry, Geophysics, Geosystems*, *4*(5), 8905. https://doi.org/10.1029/2002GC000392
Kameda, J., Inoue, S., Tanikawa, W., Yamaguchi, A., Hamada, Y., Hashimoto, Y., & Kimura, G. (2017). Alteration and dehydration of subducting oceanic crust within subduction zones: Implications for décollement step-down and plate-boundary seismogenesis. *Earth, Planets and Space*, *69*(1), 52.
Kerrick, D. M., & Connolly, J. A. D. (2001). Metamorphic devolatilization of subducted marine sediments and the transport of volatiles into the Earth's mantle. *Nature*, *411*, 293–296.
Kimura, G., & Ludden, J. (1995). Peeling oceanic crust in subduction zones. *Geology*, *23*(3), 217–220.
Kitamura, Y., & Kimura, G. (2012). Dynamic role of tectonic mélange during interseismic process of plate boundary mega earthquakes. *Tectonophysics*, *568*, 39–52.
Konstantinovskaya, E., & Malavieille, J. (2011). Thrust wedges with décollement levels and syntectonic erosion: A view from analog models. *Tectonophysics*, *502*(3–4), 336–350.
Kotowski, A. J., & Behr, W. M. (2019). Length scales and types of heterogeneities along the deep subduction interface: Insights from exhumed rocks on Syros Island, Greece. *Geosphere*, *15*(4), 1038–1065.
Kurashimo, E., Iwasaki, T., Iidaka, T., Kato, A., Yamazaki, F., Miyashita, K., & Hirata, N. (2013). Along-strike structural changes controlled by dehydration-related fluids within the Philippine Sea plate around the segment boundary of a megathrust earthquake beneath the Kii peninsula, southwest Japan. *Geophysical Research Letters*, *40*(18), 4839–4844. https://doi.org/10.1002/grl.50939
Lattard, D., & Le Breton, N. (1994). The P-T-f_{O_2} stability of Deerite, $Fe_{12}^{2+}Fe_6^{3+}[Si_{12}O_{40}](OH)_{10}$. *Contributions to Mineralogy and Petrology*, *115*(4), 474–487.
Lay, T., Kanamori, H., Ammon, C. J., Koper, K. D., Hutko, A. R., Ye, L., & Rushing, T. M. (2012). Depth-varying rupture properties of subduction zone megathrust faults. *Journal of Geophysical Research*, *117*, B04311. https://doi.org/10.1029/2011JB009133
Lay, T., Kanamori, H., Ammon, C. J., Nettles, M., Ward, S. N., Aster, R. C., & Sipkin, S. (2005). The great Sumatra-Andaman earthquake of 26 December 2004. *Science*, *308*(5725), 1127–1133.
Litchfield, N., Ellis, S., Berryman, K., & Nicol, A. (2007). Insights into subduction-related uplift along the Hikurangi Margin, New Zealand, using numerical modeling. *Journal of Geophysical Research*, *112*(F2), F02021. https://doi.org/10.1029/2006JF000535
Luo, Y., & Ampuero, J.-P. (2018). Stability of faults with heterogeneous friction properties and effective normal stress. *Tectonophysics*, *733*, 257–272. http://dx.doi.org/10.1016/j.tecto.2017.11.006
Macdonald, J. H. J., Harper, G. D., & Zhu, B. (2006). Petrology, geochemistry, and provenance of the Galice Formation, Klamath Mountains, Oregon and California. *Geological Society of America Special Paper*, *410*, 77–101.
Mason, E., Edmonds, M., & Turchyn, A. V. (2017). Remobilization of crustal carbon may dominate volcanic arc emissions. *Science*, *357*(6348), 290–294.
Menant, A., Angiboust, S., Gerya, T., Lacassin, R., Simoes, M., & Grandin, R. (2020). Transient stripping of subducting slabs controls periodic forearc uplift. *Nature Communications*, *11*(1), 1–10.
Meneghini, F., Marroni, M., Moore, J., Pandolfi, L., & Rowe, C. (2009). The processes of underthrusting and underplating in the geologic record: Structural diversity between the Franciscan Complex (California), the Kodiak Complex (Alaska) and the Internal Ligurian Units (Italy). *Geological Journal*, *44*(2), 126–152.
Middelburg, J. J., Van Der Weijden, C. H., & Woittiez, J. R. W. (1988). Chemical processes affecting the mobility of major, minor and trace elements during weathering of granitic rocks. *Chemical Geology*, *68*, 253–273.
Monie, P., & Agard, P. (2009). Coeval blueschist exhumation along thousands of kilometers: Implications for subduction channel processes. *Geochemistry, Geophysics, Geosystems*, *10*(7), Q07002. https://doi.org/10.1029/2009GC002428
Mortimer, N., & Coleman, R. G. (1985). A Neogene structural dome in the Klamath Mountains, California and Oregon. *Geology*, *13*, 253–256.
Nakano, M., Hori, T., Araki, E., Kodaira, S., & Ide, S. (2018). Shallow very-low-frequency earthquakes accompany slow slip events in the Nankai subduction zone. *Nature Communications*, *9*(1), 1–8.
Nedimović, M. R., Hyndman, R. D., Ramachandran, K., & Spence, G. D. (2003). Reflection signature of seismic and aseismic slip on the northern Cascadia subduction interface. *Nature*, *424*(6947), 416–420.
Obara, K., & Hirose, H. (2006). Non-volcanic deep low-frequency tremors accompanying slow slips in the southwest Japan subduction zone. *Tectonophysics*, *417*(1–2), 33–51.
Passchier, C. W., & Trouw, R. A. (2005). *Microtectonics*. Springer Science & Business Media.
Pearce, J. A., & Norry, M. J. (1979). Petrogenetic implications of Ti, Zr, Y, and Nb variations in volcanic rocks. *Contributions to Mineralogy and Petrology*, *69*(1), 33–47.
Pessagno, E. A. (2006). Faunal evidence for the tectonic transport of Jurassic terranes in Oregon, California, and Mexico. *Geological Society of America Special Paper*, *410*, 31–52.
Platt, J. P. (2015). Origin of Franciscan blueschist-bearing melange at San Simeon, central California coast. *International Geology Review*, *57*(5–8), 843–853.
Plunder, A., Agard, P., Chopin, C., & Okay, A. I. (2013). Geodynamics of the Tavşanlı zone, western Turkey: Insights into subduction/obduction processes. *Tectonophysics*, *608*, 884–903.
Plunder, A., Agard, P., Dubacq, B., Chopin, C., & Bellanger, M. (2012). How continuous and precise is the record of P–T paths? Insights from combined thermobarometry and thermodynamic modelling into subduction dynamics (Schistes Lustrés, W. Alps). *Journal of Metamorphic Geology*, *30*(3), 323–346.
Rogers, G., & Dragert, H. (2003). Episodic tremor and slip on the Cascadia subduction zone: The chatter of silent slip. *Science*, *300*(5627), 1942–1943.
Rowe, C. D., Moore, J. C., Remitti, F., & Scientists, I. E. T. (2013). The thickness of subduction plate boundary faults from the seafloor into the seismogenic zone. *Geology*, *41*(9), 991–994.

Ruh, J. B. (2020). Numerical modeling of tectonic underplating in accretionary wedge systems. *Geosphere*, *16*(6), 1385–1407.
Ruh, J. B., Kaus, B. J., & Burg, J.-P. (2012). Numerical investigation of deformation mechanics in fold-and-thrust belts: Influence of rheology of single and multiple décollements. *Tectonics*, *31*(3), TC3005. https://doi.org/10.1029/2011TC003047
Ruh, J. B., Le Pourhiet, L., Agard, P., Burov, E., & Gerya, T. (2015). Tectonic slicing of subducting oceanic crust along plate interfaces: Numerical modeling. *Geochemistry, Geophysics, Geosystems*, *16*(10), 3505–3531. https://doi.org/10.1002/2015GC005998
Rutter, E. (1976). A discussion on natural strain and geological structure-the kinetics of rock deformation by pressure solution. *Philosophical Transactions of the Royal Society of London - Series A: Mathematical and Physical Sciences*, *283*(1312), 203–219.
Saffer, D. M., & Wallace, L. M. (2015). The frictional, hydrologic, metamorphic and thermal habitat of shallow slow earthquakes. *Nature Geoscience*, *8*(8), 594–600.
Sage, F., Collot, J. Y., & Ranero, C. R. (2006). Interplate patchiness and subduction-erosion mechanisms: Evidence from depth-migrated seismic images at the central Ecuador convergent margin. *Geology*, *34*(12), 997–1000.
Saleeby, J. B. (1990). Geochronological and tectonostratigraphic framework of Sierran-Klamath ophiolitic assemblages. *Geological Society of America Special Paper*, *255*, 93–114.
Saleeby, J. B., & Harper, G. D. (1993). Tectonic relations between the Galice formation and the Condrey Mountain Schist, Klamath Mountains, northern California. In *Mesozoic Paleogeography of the Western United States-II. Pacific Section SEPM. No.71*. (pp. 61–80). Los Angeles, CA: Society of Economic Paleontologists and Mineralogists.
Shelly, D. R., Beroza, G. C., Zhang, H., Thurber, C. H., & Ide, S. (2006). High-resolution subduction zone seismicity and velocity structure beneath Ibaraki Prefecture, Japan. *Journal of Geophysical Research: Solid Earth*, *111*(B6), 1–10. http://dx.doi.org/10.1029/2005jb004081
Shervais, J. W. (1982). Ti-V plots and the petrogenesis of modern and ophiolitic lavas. *Earth and Planetary Science Letters*, *59*(1), 101–118.
Snoke, A. W., & Barnes, C. G. (2006). The development of tectonic concepts for the Klamath Mountains province, California and Oregon. *Geological Society of America Special Paper*, *410*, 1–29.
Stöckhert, B., Wachmann, M., Küster, M., & Bimmermann, S. (1999). Low effective viscosity during high pressure metamorphism due to dissolution precipitation creep: The record of HP–LT metamorphic carbonates and siliciclastic rocks from Crete. *Tectonophysics*, *303*(1–4), 299–319.
Tarling, M. S., Smith, S. A., & Scott, J. M. (2019). Fluid overpressure from chemical reactions in serpentinite within the source region of deep episodic tremor. *Nature Geoscience*, *12*, 1034–1042.
Todd, E. K., Schwartz, S. Y., Mochizuki, K., Wallace, L. M., Sheehan, A. F., Webb, S. C., et al. (2018). Earthquakes and tremor linked to seamount subduction during shallow slow slip at the Hikurangi margin, New Zealand. *Journal of Geophysical Research: Solid Earth*, *123*(8), 6769–6783. https://doi.org/10.1029/2018JB016136
Tulley, C. J., Fagereng, A., & Ujiie, K. (2020). Hydrous oceanic crust hosts megathrust creep at low shear stresses. *Science Advances*, *6*(22), 1–9.
Ujiie, K., Saishu, H., Fagereng, Å., Nishiyama, N., Otsubo, M., Masuyama, H., & Kagi, H. (2018). An explanation of episodic tremor and slow slip constrained by crack-seal veins and viscous shear in subduction mélange. *Geophysical Research Letters*, *45*(11), 5371–5379. https://doi.org/10.1029/2018GL078374
Vogt, K., & Gerya, T. (2014). Deep plate serpentinization triggers skinning of subducting slabs. *Geology*, *42*(8), 723–726.
Von Huene, R., & Scholl, D. W. (1991). Observations at convergent margins concerning sediment subduction, subduction erosion, and the growth of continental crust. *Reviews of Geophysics*, *29*(3), 279–316.
Wakabayashi, J. (1990). Counterclockwise PTt paths from amphibolites, Franciscan Complex, California: Relics from the early stages of subduction zone metamorphism. *The Journal of Geology*, *98*(5), 657–680.
Wright, J. E. (1982). Permo-Triassic accretionary subduction complex, southwestern Klamath Mountains, northern California. *Journal of Geophysical Research*, *87*(B5), 3805–3818.
Wright, J. E., & Wyld, S. J. (1994). The Rattlesnake Creek terrane, Klamath Mountains, California: An early Mesozoic volcanic arc and its basement of tectonically disrupted oceanic crust. *Geological Society of America Bulletin*, *106*(8), 1033–1056.
Yamato, P., Kaus, B. J., Mouthereau, F., & Castelltort, S. (2011). Dynamic constraints on the crustal-scale rheology of the Zagros fold belt, Iran. *Geology*, *39*(9), 815–818.
Yule, J. D., Saleeby, J. B., & Barnes, C. G. (2006). A rift-edge facies of the Late Jurassic Rogue-Chetco arc and Josephine ophiolite, Klamath Mountains, Oregon. *Geological Society of America Special Paper*, *410*, 53–76.